Guo *et al. Journal of Nanobiotechnology (2025) 23:303*
https://doi.org/10.1186/s12951-025-03315-z

Journal of Nanobiotechnology

RESEARCH

Open Access

PTEN as a prognostic factor for radiotherapy plus immunotherapy response in nasopharyngeal carcinoma

Jiaxing Guo[1†], Ming Zhang[2†], Xiaoli Li[2*] and Jiashuo Wang[1*]

Abstract

Background In the context of nasopharyngeal carcinoma (NPC) treatment, radiotherapy combined with immunotherapy (IR + RT) is gaining traction. This study focuses on analyzing exosomal proteins, particularly Phosphatase and Tensin Homolog (PTEN), for predicting the efficacy of NPC treatments. Serum samples from NPC patients and IR + RT recipients were utilized for exosome (Exo) extraction and subsequent transcriptomic and proteomic analyses to identify treatment-related proteins. Flow cytometry of cells and exosomal analysis were performed to examine these proteins. In vitro experiments using C666-1 cells and their Exos explored various cellular responses, while a murine subcutaneous NPC model investigated the impact of PTEN modulation on tumor growth and the immune microenvironment.

Results The study demonstrated that PTEN serves as a crucial predictive biomarker, with its expression changes correlated with M2 macrophage polarization and CD8+ T cell activity. This highlights the potential significance of PTEN in predicting treatment outcomes and influencing the immune response in NPC.

Conclusion The findings suggest that PTEN could play a key role in enhancing the efficacy of NPC radiotherapy and immunotherapy. By shedding light on PTEN's impact on tumor growth and the immune microenvironment, this study lays the groundwork for future personalized therapeutic strategies in NPC treatment.

Keywords Nasopharyngeal carcinoma, Radiotherapy, Immunotherapy, Nanofluidic technology, Machine learning, Tumor microenvironment, Phosphatase and Tensin Homolog, Exosome

---

[†] Jiaxing Guo and Ming Zhang are regarded as co-first authors.

*Correspondence:
Xiaoli Li
18900913351@163.com
Jiashuo Wang
sayerswond929@163.com

Graphical abstract

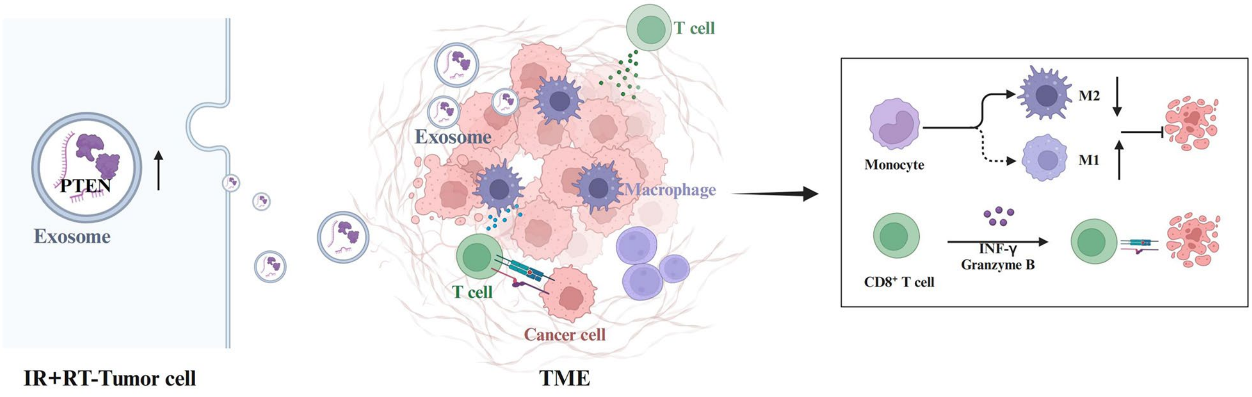

Introduction

Nasopharyngeal carcinoma (NPC) is a malignant tumor characterized by significant geographic and ethnic disparities in incidence, with notably higher rates in Southeast Asia and Southern China [1–3]. The principal treatment modalities for NPC include radiotherapy, chemotherapy, and, more recently, immunotherapy [4–6]. Despite advances in treatment options, the five-year survival rate for NPC patients has not significantly improved, partly due to substantial individual variations in treatment response [7, 8]. Radiotherapy combined with Immunotherapy (RT + IT) is a critical strategy in NPC treatment, yet assessing its effectiveness remains challenging [9]. The lack of effective biomarkers hampers accurate prediction of treatment outcomes, thereby affecting the selection and adjustment of therapeutic strategies [10].

Recent advances in biotechnology, especially the application of nanofluidic technology and machine learning, have provided new methodologies for analyzing complex biological samples [11–13]. Nanofluidic technology, known for its high sensitivity and throughput, is particularly suitable for detecting minute biomarkers in body fluids. Moreover, machine learning has demonstrated substantial potential in processing biological information and pattern recognition, offering a new perspective for data-driven disease diagnosis and prediction of treatment outcomes [11–13]. Integrating these technologies to screen and analyze exosomal proteins in NPC treatment can significantly enhance biomarker identification accuracy and predictive power [14, 15].

Exosomes (exos) are small vesicles released into the extracellular environment by cells, containing proteins, RNA, and DNA, and are crucial sources of disease biomarkers [16, 17]. In NPC, exos modulate the tumor microenvironment, influencing tumor development and response to therapy [18–20]. Particularly, the Phosphatase and Tensin Homolog (PTEN) protein, a significant tumor suppressor, is closely associated with the proliferation, migration, and invasion capabilities of cancer cells across various cancers [21–23]. Furthermore, PTEN also regulates cells within the immune system, such as T cells and macrophages, affecting the outcome of immunotherapy [24–26]. Therefore, the expression of PTEN protein and its presence in exos may serve as a critical indicator for predicting the efficacy of radiotherapy and immunotherapy in NPC [27].

Although current research has revealed the potential role of exos in cancer therapy, studies on their ability to accurately predict treatment outcomes in clinical settings remain limited [28]. Moreover, much of the research has focused on analyzing single biomarkers, overlooking the complexity and dynamic changes within the tumor microenvironment. Existing technologies also have not fully exploited the richness of information within exos, particularly in terms of comprehensive proteomic analysis [29–31]. Consequently, there is a need for a systematic approach that integrates advanced technologies to thoroughly assess the potential applications of exosomal proteins in the treatment of NPC [32–34].

This study aims to utilize nanofluidic technology and machine learning to select and analyze exosomal proteins, especially PTEN, from the serum of NPC patients to predict the efficacy of RT + IT. Through precise biomarker identification and functional validation, we hope to provide a scientific basis for personalized treatment of NPC, optimize treatment protocols, and enhance the accuracy of treatment outcome predictions. Additionally, the results are expected to deepen our understanding of the regulatory mechanisms within the NPC tumor microenvironment, potentially leading to the development of new therapeutic targets. From a clinical perspective, the findings of this study are likely to enhance the individualization of NPC treatment, ultimately improving patient prognosis and quality of life.

Materials and methods

Patient samples and ethical statement

Serum samples were collected from six NPC patients and six patients who received IR + RT treatment at our hospital from January 2022 to December 2023. Samples were taken at diagnosis and post-treatment. After collection, serum samples were allowed to clot at room temperature for 30 min, then centrifuged at 3000×*g* for 10 min to separate the serum. The serum was transferred to sterile centrifuge tubes and stored at − 80 °C to prevent biomarker degradation until analysis. Patient details are presented in Table S1. Written informed consent was obtained from all participants, and the study was approved by our institution's Scientific Research Ethics Committee.

Isolation and purification of exos

Exos were prepared and purified using a previously described exo Trajectory Etching Magnetic Nanopore (ExoTENPO) chip, following protocols from the literature. Serum samples from six NPC patients and six IR + RT NPC patients were processed using nanofluidic technology. Before exo isolation, all samples were vortexed to resuspend exos that might have aggregated due to freezing conditions. Magnetic labeling was performed using antibiotic ultrapure microbeads (130-090-485, Miltenyi Biotec, Germany) and biotinylated antibodies. Human-specific biotinylated anti-CD9 (13-0098-80, ThermoFisher, USA), anti-CD63 (353017, BioLegend, USA), and custom biotinylated anti-CD81 antibodies (BioLegend, USA) were used. Initially, 2.5 µL of biotinylated antibody was added per 20 mL of culture medium or 1 mL of plasma, and the sample was incubated at room temperature for 20 min. Then, antibiotic ultrapure microbeads were added, and the mixture was incubated at room temperature for another 20 min. Subsequently, the sample was placed into the storage reservoir of the ExoTENPO chip, and negative pressure was applied using a programmable syringe pump (Braintree Scientific). As the sample passed through the chip, magnetically labeled exos were captured at the edges of the chip pores.

Transmission electron microscopy (TEM)

Exos were fixed in 2.5% glutaraldehyde in PBS for 2 h, washed, and ultracentrifuged. The pellet was resuspended in 100 µL of PBS, and 20 µL of this suspension was placed onto a carbon-coated grid. The samples were then negatively stained with a 3% aqueous solution of phosphotungstic acid (79690, Sigma, USA) for 1 min and examined under a TEM (JEM-1230, JEOL, Tokyo, Japan).

Nanoparticle tracking analysis (NTA)

Exos from each group were resuspended in PBS and diluted 500 times using Milli-Q water. The diluted exos were then loaded into the sample chamber of the NanoSight LM10 (Malvern, UK) using a sterile syringe, ensuring the absence of air bubbles until the chamber was full. Videos were analyzed using NanoSight version 2.3 software (Malvern, UK).

Western blot (WB) for exosomal surface markers

Exos were resuspended in RIPA lysis buffer (P0013C, Beyotime, China) and analyzed via WB to identify exosomal markers CD81, CD63, Alix, and the endoplasmic reticulum marker Calnexin. Refer to the WB section for details on the antibody. Each experiment was conducted in triplicate.

High-throughput transcriptomic sequencing data acquisition

Serum exo samples from three NPC patients (NPC exo) and three patients who underwent RT + IT (RT + IT-NPC exo) were immediately transported to the laboratory for sample processing and RNA extraction. According to the manufacturer's instructions, total RNA was extracted from each sample using Trizol reagent (Catalog No. 16096020, ThermoFisher, New York, USA). RNA concentration, purity, and integrity were assessed using a Qubit® 2.0 Fluorometer® (Q33216, Life Technologies, CA, USA) with a Qubit® RNA Assay Kit (HKR2106-01, Shanghai Biogene Biotech, China), a Nanodrop spectrophotometer (IMPLEN, CA, USA), and an RNA Nano 6000 Assay Kit (5067-1511) on the Bioanalyzer 2100 system. Upon meeting the experimental standards for concentration, purity, and integrity, 3 µg of total RNA from each sample was used as input material for RNA library preparation. Libraries were prepared using the NEBNext® UltraTM RNA Library Prep Kit (E7435L, NEB, Beijing) for Illumina® (The state of Nebraska, USA), recommended by the manufacturer, and their quality was evaluated on an Agilent Bioanalyzer 2100 system. Indexed samples were clustered using the TruSeq PE Cluster Kit v3 cBot HS

(PE-401-3001, Illumina) on a cBot clustering system. Following cluster generation, libraries were sequenced on an Illumina HiSeq 550 platform.

Quality control of high-throughput sequencing data

The quality of raw paired-end sequencing reads was checked using FastQC software v0.11.8. Raw data preprocessing was performed with Cutadapt software 1.18 to remove Illumina sequencing adapters and poly (A) tails. Reads with an N-content exceeding 5% were removed using a Perl script. The FASTX-Toolkit software 0.0.13 was employed to retain reads, with at least 70% of bases having a quality score above 20. Paired-end sequences were repaired using BBMap software. Finally, filtered high-quality reads were aligned to the human genome using HISAT2 software (version 0.7.12).

Transcriptomic sequencing data bioinformatics analysis

Differentially expressed genes (DEGs) between NPC exo samples and RT + IT-NPC exo samples were identified using the Xiantao academic website with a threshold of $|\log2FC| > 2$ and $p\text{-value} < 0.05$. Volcano plots and heatmaps were generated to visualize these DEGs.

Proteomics sample preparation and analysis

Proteomic analysis of exos from the serum of NPC patients (NPC exo, n = 6) and patients post-RT + IT (RT + IT-NPC exo, n = 6) was conducted using nanofluidic technology. Initially, exos were isolated and purified using the previously described methods. Exos from the serum of NPC patients (both NPC exo and RT + IT-NPC exo samples) were subjected to cryogrinding, and the resultant powder was transferred to 5 cm3 centrifuge tubes. The samples underwent ultrasonic disruption in an ice bath using a sonicator (SCIENTZ-IID, Scientz, Ningbo, China) in an extraction buffer containing 10 mM DTT (R0861, MBI, Beijing, China), 1% protease inhibitor mixture (P6731, Solarbio, Beijing, China), and 2 mM EDTA (E1170, Solarbio, Beijing, China) in phenol (100206, Merck, USA). This step was repeated eight times. Subsequently, an equal pH 8.0 Tris-saturated phenol (HC1380, BIOFOUNT, Beijing, China) was added, followed by vortexing for 4 min. The samples were centrifuged at 5000 × g for 10 min at 4 °C, and the phenolic layer was transferred to a new centrifuge tube. To the phenolic solution, 0.1 M ammonium sulfate (101217, Merck, USA) saturated methanol (106035, Merck, USA) was added in a 1:5 volume ratio and left overnight to precipitate proteins. After centrifugation at 4 °C for 10 min, the supernatant was discarded. The remaining residue was washed once with ice-cold methanol and three times with ice-cold acetone. The washed protein was redissolved in 8 M urea (U8020, Solarbio, Beijing, China), and the protein concentration was determined using a BCA kit (23227, ThermoFisher, USA), following the manufacturer's instructions.

Proteolysis, peptide labeling, and nano-LC–MS/MS analysis

For each sample, 50 μg of protein was subjected to enzymatic digestion. The protein solution was first mixed with DTT to achieve a final concentration of 5 mM and incubated at 56 °C for 30 min. Acetamide was added to a final concentration of 11 mM, and the mixture was allowed to stand at room temperature for 15 min. Subsequently, the urea concentration in the sample was diluted to below 2 M, and trypsin (25200056, Thermo Fisher Scientific, USA) was added at a 1:50 (w/w) enzyme-to-protein ratio, followed by overnight incubation at 37 °C. Additional trypsin was added at a 1:100 enzyme-to-protein ratio, and the digestion continued for 4 h.

Following trypsin digestion, peptides were desalted using HyperSep™ C18 columns (60108-302, Thermo Fisher Scientific, USA) and vacuum dried. The peptides were redissolved in 0.5 M TEAB (90114, Thermo Fisher Scientific, USA) and processed according to the manufacturer's instructions provided with the TMT reagent kit (90064CH, Thermo Fisher Scientific, USA). Briefly, a unit of TMT reagent was thawed and reconstituted in acetonitrile (113212, Merck, USA). The peptide mixture was incubated at room temperature for 2 h, then desalted and dried using a vacuum centrifuge. The labeled peptides from each group were mixed in equal amounts and fractionated using a Pierce™ High pH Reverse-Phase Peptide Fractionation Kit (84868, Thermo Fisher Scientific, USA). The fractions were collected and combined into 15 components, and each component was dried and redissolved in 0.1% formic acid (159002, Merck, USA).

Each sample was subjected to 2 μg of peptides separated on a nano-UPLC system, the Easy nLC 1200 (Thermo Fisher Scientific, USA). The samples were first loaded onto a Trap C18 column (100 μm × 20 mm, 5 μm) and then separated on an analytical C18 column (75 μm × 150 mm, 3 μm) with a flow rate of 300 nL/min. The mobile phase A consisted of 0.1% formic acid in water, and mobile phase B consisted of 0.1% formic acid in acetonitrile (95% acetonitrile). The gradient elution program was as follows: 0–2 min, 2% to 8% B; 2–71 min, 8% to 28% B; 71–79 min, 28% to 40% B; 79–81 min, 40% to 100% B; 81–90 min, maintained at 100% B. The eluted peptides were analyzed by a Q-Exactive HFX mass spectrometer (Thermo Fisher Scientific, USA). The analysis lasted 60 min, with an electrospray voltage of 2.1 kV. The detection mode was positive ion, with a parent ion scan range of 350–1200 m/z. The primary mass spectrometry resolution was 60,000 @ m/z 200, AGC target: 3e6, maximum IT: 30 ms. Secondary mass spectrometry resolution: 15,000 @ m/z 200, AGC target: 1e6, maximum IT: 25 ms, MS2 Activation Type: HCD, Isolation window: 20 Th, and Normalized collision energy: 32.

Database retrieval and data processing

LC–MS/MS data were processed using MaxQuant software (v.1.5.2.8), including peptide identification and protein quantification. Searches were conducted against the UniProt 14.1 (2009) Gossypium hirsutum and reverse decoy databases. Trypsin/P was specified as the cleavage enzyme with allowance for up to two missed cleavages. The initial search tolerance was set at 20 ppm, with the main search at 5 ppm and a fragment ion mass tolerance of 0.02 Da. The search was validated with a peptide false discovery rate (FDR) ≤ 0.01 and protein FDR ≤ 0.01, and peptide score distribution was used as a filtering criterion. Differentially expressed proteins (DEPs) between samples were identified using the "Limma" package in R, with a threshold of $|\log2FC| > 1$ and p-value < 0.05, and differential expression was visualized using volcano plots and heatmaps.

Machine learning for feature gene selection

Feature genes were selected from DEGs using a least absolute shrinkage and selection operator (LASSO) logistic regression analysis performed with the "glmnet" package in R, applying a binomial logistic regression. The minimum binomial deviation determined the optimal penalty parameter λ. In the support vector machine-recursive feature elimination (SVM-RFE) process, the "e1071" package in R was used to identify optimal variables, while the "kernlab" and "caret" packages were utilized to select the minimum cross-validation error. Genes identified by both algorithms were intersected to filter out characteristic genetic biomarkers.

Receiver operating characteristic (ROC) curve analysis

The ROC curves were plotted, and the area under the curve (AUC) was calculated using the "pROC" package in R. This analysis assessed the predictive utility of the identified biomarkers.

Lentiviral infection

Lentiviral packaging services were provided by Sangon Biotech (Shanghai, China). The pHAGE-puro vector series, along with helper plasmids pSPAX2 and pMD2.G and the pSuper-retro-puro vector series with helper plasmids gag/pol and VSVG, were co-transfected into HEK293T cells (Catalog No: CRL-11268, purchased from ATCC, USA). 48 h post-transfection, the supernatant was collected and filtered through a 0.45 μm filter. The virus was collected again after 72 h, centrifuged to concentrate, and the viruses from both collections were mixed and titrated. For lentiviral-mediated transduction, cells were seeded in 6-well plates and infected with the packaged virus (MOI = 10, working titer approximately 2 × 109 TU/mL) supplemented with 5 μg/mL polybrene (Merck, TR-1003, USA). Four hours post-infection, an equal medium volume was added to dilute the polybrene, and the medium was replaced with fresh culture medium after 24 h. For the generation of stable cell lines, cells were selected with 10 μg/mL puromycin (Sangon Biotech, E607054, Shanghai, China). Silencing lentiviral sequences are listed in Table S2, and sequences with superior silencing efficacy were selected for further experiments.

Cell culture

C666-1 cells (SNLM-516, SUNNCELL, China) were cultured in RPMI 1640 medium (R4130, Sigma, USA) supplemented with 10% FBS (F8318, Sigma, USA), 1% penicillin and streptomycin (V900929, Sigma, USA) at 37 °C in a 5% CO2 incubator.

For radiotherapy, C666-1 cells were exposed to vertical radiation from a Varian™ TRUEBEAM™ linear accelerator, receiving a localized dose of 6 Gy at a radiation intensity of 400 cGy/min for 1 min. For immunotherapy, C666-1 cells were co-cultured with Nivolumab (T9907, TargetMol, USA) at a concentration of 10 μM for 24 h.

Cells were randomly divided into the Control and RT + IT groups (cells subjected to RT + IT). The RT + IT group was further divided into four subgroups: PBS group (cells treated with PBS), RT + IT exo group (cells treated with exos from cells subjected to RT + IT), sh-NC + RT + IT exo group (cells treated with non-targeting control shRNA and exos from RT + IT), and sh-PTEN + RT + IT exo group (cells with PTEN knockdown treated with exos from RT + IT).

Subcutaneous xenograft model

huHSC-C-NKG-ProF mice (6 to 8 weeks old) (Cyagen, USA) were housed in a specific pathogen-free environment. All mouse experiments were conducted in accordance with institutional guidelines and approved by our Institutional Animal Care and Use Committee. A subcutaneous xenograft model was established by injecting 1 × 106 C666-1 cells mixed with an equal volume of Matrigel subcutaneously into humanized mice. When tumor volumes reached 100 mm3 for radiotherapy, a localized dose of 8 Gy at 600 cGy/min was administered daily for 1 min [35]. For immunotherapy, Nivolumab (5 mg/kg, twice weekly) was administered intraperitoneally for four consecutive weeks after tumor implantation [36]. For Exo treatment, Exos (20 μg of total protein in 200 μL of PBS) was injected intravenously every five days for six doses, starting after cell injection. Tumor growth, body weight, and signs of illness were monitored every five days using calipers, and all mice were euthanized 30 days post-tumor inoculation [37].

Mice were randomly divided into the following groups: Control group, RT + IT group (mice receiving RT + IT); the RT + IT group was further subdivided into four subgroups: PBS group (mice treated with PBS), RT + IT exo group (mice treated with exos from cells subjected to RT + IT), sh-NC + RT + IT exo group (mice treated with non-targeting control shRNA and exos from RT + IT), and sh-PTEN + RT + IT exo group (mice with PTEN knockdown treated with exos from RT + IT).

Uptake of exos by tumor cells

C666-1 cells were seeded at a density of 5 × 105 cells/well on cell culture slides and grown to 75% confluence. Following the manufacturer's instructions, Cy5.5 (HY-D0924, MedChemExpress, USA) was mixed with RT + IT exo (5 μg/ml), sh-NC + RT + IT exo (5 μg/ml), and sh-PTEN + RT + IT exo (5 μg/ml), resulting in Cy5.5-labeled exos. These exos were then co-cultured with C666-1 cells for 24 h. The cell nuclei were stained with DAPI (C1002, Beyotime, China), and the slides were washed three times before DAPI staining. Images were captured using an Olympus IX81 fluorescence microscope and analyzed using Image J software. Following the manufacturer's instructions,

Tumor targeting specificity of exo

To evaluate the in vivo targeting capability of cell-derived exos towards tumor cells, Cy5.5-labeled exos (RT + IT exo, sh-NC + RT + IT exo, sh-PTEN + RT + IT exo) were prepared according to the manufacturer's instructions (HY-D0924, MCE). Post-injection, tissues from the tumor, heart, liver, spleen, lung, and kidney were dissected, and fluorescence images of the Cy5.5-labeled exos were captured using the IVIS Spectrum Imaging System (PerkinElmer, Waltham, MA, USA) [38, 39].

RT-qPCR analysis of target gene expression

Total RNA was extracted from tissues or cells using Trizol reagent (15596026, ThermoFisher, USA), and its concentration and purity were measured at 260/280 nm using a NanoDrop LITE spectrophotometer (ND-LITE-PR, ThermoFisher, USA). cDNA synthesis was performed using the PrimeScript RT reagent Kit with gDNA Eraser (RR047Q, TaKaRa, Japan). RT-qPCR was conducted on the 7500 Fast Real-Time PCR System (4351106, ThermoFisher, USA) under the following conditions: 95 °C for 10 min, followed by 40 cycles of 95 °C for 10 s, 60 °C for 20 s, and 72 °C for 34 s. TaKaRa (Table S3) synthesized primers for each gene, with GAPDH as the internal control. Relative gene expression was analyzed using the 2−ΔΔCt method, where ΔΔCt = (Average Ct of the target gene in the experimental group − Average Ct of housekeeping gene in the experimental group) − (Average Ct of the target gene in the control group − Average Ct of housekeeping gene in the control group). All RT-qPCR assays were performed in triplicate.

WB

Total protein was extracted from tissues using RIPA lysis buffer containing PMSF (P0013C, Beyotime, China), incubated on ice for 30 min, and then centrifuged at 8000*g* for 10 min at 4 °C to collect the supernatant. Protein concentration was determined using a BCA Protein Assay Kit (23227, ThermoFisher, USA). Samples containing 50 μg of protein were resolved in 2 × SDS sample buffer and boiled at 100 °C for 5 min. Proteins were then separated by SDS-PAGE and transferred onto a PVDF membrane (88,518, ThermoFisher, USA). The membrane was blocked with 5% BSA (9048-46-8, Sigma-Aldrich, USA) at room temperature for 1 h and incubated overnight at 4 °C with diluted primary antibodies against CD63 (ab315108, 1:1000, Abcam, UK), CD81 (ab109201, 1:1000, Abcam, UK), Alix (ab275377, 1:1000, Abcam, UK), Calnexin (ab22595, 1:1000, Abcam, UK), GAPDH (ab181602, 1:10,000, Abcam, UK), and PTEN (ab267787, 1:1000, Abcam, UK). After washing thrice with TBST for 10 min each, the membrane was incubated with HRP-conjugated secondary antibodies: goat anti-rabbit IgG H&L (ab97051, 1:2000, Abcam, UK) and goat anti-mouse IgG (ab205719, 1:2000, Abcam, UK) for 1 h. After rinsing with TBST, the membrane was placed on a clean glass plate. Solutions A and B from the ECL WB Substrate Kit (abs920, Absin Bioscience Inc., Shanghai, China) were mixed and applied to the membrane in a dark room. Protein bands were visualized using the Bio-Rad Imaging System (Bio-Rad, USA) and analyzed with Quantity One v4.6.2 software. Relative protein levels were quantified based on the grayscale intensity of the target protein bands normalized to GAPDH. The experiment was conducted in triplicate, and results were averaged.

EdU incorporation assay

Well-grown CD8+ T cells and C666-1 cells were incubated with 10 μmol/L EdU solution (ST067, Beyotime, China) for 2 h in a culture incubator. The medium was then aspirated, and the cells were fixed with 4% paraformaldehyde in PBS at room temperature for 15 min, followed by two washes with 3% BSA in PBS. Cells were permeabilized with 0.5% Triton X-100 in PBS for 20 min at room temperature, washed twice with 3% BSA in PBS, and then stained with 100 μL of detection solution per well in the dark at room temperature for 30 min. Nuclei were stained with DAPI (C1002, Beyotime, China) for 5 min, and cells were examined under a fluorescence microscope (Model: FM-600, Shanghai Pudan Optical Instrument Co., Ltd.) across 6–10 random fields. Positive cell counts were recorded, and the EdU incorporation rate was calculated as (Number of EdU-positive cells/(Number of EdU-positive cells + Number of EdU-negative cells)) × 100%. Each experiment was performed in triplicate.

Flow cytometry for apoptosis detection

Cells and tumor tissues from various groups were collected, and apoptosis was assessed using an Annexin V-FITC Apoptosis Detection Kit (C1062M, Beyotime, China). Collected cells were stained with Annexin V and PI in 1 × binding buffer at room temperature for 15 min. Stained cells were analyzed on a FACSCelesta flow cytometer (BD Biosciences, San Jose, CA, USA) equipped with FlowJo V10 software (FlowJo, OH, USA). Apoptotic cells were identified in the Q2 and Q3 quadrants, with late apoptotic cells in Q2 and early apoptotic cells in Q3.

Colony formation assay

Cells were washed twice with PBS (P2272, Sigma, USA) and digested with trypsin (T2600000, Sigma, USA). Single-cell suspensions were prepared by resuspending in a complete medium. Cell suspensions (2 mL at 500 cells/mL) were seeded into six-well plates and gently agitated to ensure even distribution. Cells were cultured at 37 °C with 5% CO2 for 7–14 days until visible white colonies formed. After two PBS washes, cells were fixed with 4% paraformaldehyde (158127, Sigma, USA) and stained for 15 min with 0.5% crystal violet solution (V5265, Sigma, USA). Colonies consisting of more than 50 cells were counted under a stereo microscope.

Transwell assay

Cells were counted in a medium containing 10% FBS and adjusted to 1 × 105 cells/mL in a serum-free medium. For the invasion assay, Matrigel (354234, Corning, USA) was applied to the upper porous membrane of the Transwell. 100 μL of cell suspension was added to the upper chamber, while the lower chamber was filled with a complete medium containing 10% FBS as a chemoattractant. After 24 h at 37 °C and 5% CO2, non-invasive cells in the upper chamber were removed with a cotton swab, and cells that migrated to the lower surface were stained with 0.1% crystal violet. Five random fields were counted under an inverted microscope. Matrigel coating was omitted for the migration assay, but all other steps remained the same.

Wound healing assay

Cells from each group exhibiting good growth were prepared into single-cell suspensions using the previously described method. The cells were then counted and inoculated into six-well plates at a density of 2 mL per well (8 × 105 cells/mL). Cells were cultured at 37 °C and 5% CO2 until they reached 90%-100% confluence. A sterile 200 μL pipette tip was used to scratch two parallel lines across the well. After washing twice with PBS to remove floating cells, the cells were cultured in a serum-free medium. Photographs were taken after 24 h, and the rate of wound closure was calculated.

Hematoxylin and eosin (H&E) staining

Following the manufacturer's instructions, the tissue sections were deparaffinized to water and stained using an H&E Staining Kit (PT001, Shanghai Bogoo Biotech Co., China). The key steps included: staining with hematoxylin at room temperature for 10 min, followed by rinsing under running water for 30–60 s; differentiation in 1% hydrochloric acid in ethanol for 30 s, then a 5-min soak in running water; eosin staining at room temperature for 1 min; dehydration through an alcohol gradient (70%, 80%, 90%, 95%, and 100%), 1 min at each concentration; clearing in xylene substitute for 1 min, two changes in xylene I and II, each for 1 min; and mounting with neutral resin in a fume hood. Finally, photographs were taken using an optical microscope (BX50; Olympus Corp, Tokyo, Japan) to observe morphological changes across groups.

Immunofluorescence staining

Cells were fixed with 4% paraformaldehyde at room temperature for 15 min, washed twice with PBS, and permeabilized with 0.5% Triton X-100 (P0096, Beyotime, China) for 10 min. The cells were then incubated overnight at 4 °C with primary antibodies against CD206 (ab64693, 1:100, Abcam, UK), IL-10 (ab133575, 1:100, Abcam, UK), and Arg-1 (ab96183, 1:100, Abcam, UK). After three PBS washes, cells were incubated with Goat anti-rabbit IgG (Alexa Fluor 488) (ab150077, 1:1000, Abcam, UK) for 1 h, followed by three more PBS washes. Cells were stained with DAPI (C1002, Beyotime, China) at room temperature for 10 min. The cells were stored at 4 °C and observed under a Zeiss Axiovert 123 M fluorescence microscope (Germany). Fluorescence intensity was quantitatively analyzed using ImageJ software, averaging results from six fields per group.

Immunohistochemical staining

After embedding and sectioning, samples from each group were baked at 60 °C for 20 min. Sections were then sequentially immersed in xylene (two changes, 15 min each), absolute ethanol (two changes, 5 min each), and rehydrated in 95% and 70% ethanol for 10 min each. To block endogenous peroxidase activity, 3% H2O2 was applied to each section at room temperature for 10 min. Sections were then placed in citrate buffer and microwaved for 3 min for antigen retrieval, followed by a 10-min incubation at room temperature and three PBS washes. Blocking was performed using normal goat serum blocking solution (E510009, Sangon Biotech, Shanghai, China) at room temperature for 20 min. Primary antibodies, diluted appropriately, were added: rabbit anti-Ki67 (ab15580, 1:100, Abcam, UK), rabbit anti-PTEN (ab267787, 1:2000, Abcam, UK), rabbit anti-CD206 (ab64693, 1:100, Abcam, UK), and mouse anti-CD86 (MA1-10293, 1:100, ThermoFisher, USA). Sections were incubated overnight at 4 °C. The following day, sections were washed three times with PBS and incubated with goat anti-rabbit IgG secondary antibody (ab6721, 1:1000, Abcam, UK) for 30 min. After washing with PBS, Add one drop each of chromogens A, B, and C from the DAB Chromogen Kit (P0203, Beyotime, Shanghai, China) to the specimen, develop the color for 6 min, and then stain in hematoxylin for 30 s. Sections were dehydrated through graded ethanol (70%, 80%, 90%, 95%, and absolute ethanol, 2 min each), cleared in xylene (two changes, 5 min each), and mounted with neutral resin. Observations were made using an upright microscope (BX63, Olympus, Japan), and staining intensity in each field was quantified using ImageJ software. Six mice were analyzed for each group, with three sections per mouse and five fields per section. The average staining intensity across all fields per mouse was used as the representative value.

Macrophage culture

THP-1 cells (SCSP-567, Cell Bank of the Chinese Academy of Sciences, China) were incubated for 24 h in a medium containing 100 ng/mL PMA (P8139-10MG, Sigma-Aldrich, Shanghai, China) to differentiate into adherent THP-1 macrophages (M0 macrophages). M0 macrophages were then incubated for 48 h in a medium containing 20 ng/mL IL-4 (AF-200-04, PeproTech, USA) to obtain M2 macrophages (M2-CM). Subsequently, M0 macrophages were treated with PBS, RT + IT exo (5 μg/mL), sh-NC + RT + IT exo (5 μg/mL), or sh-PTEN + RT + IT exo (5 μg/mL) for 24 h before harvesting for analysis.

T cell culture

CD8+ T lymphocytes were purified from the spleens of C57BL/6 mice (6–8 weeks old, 213, Vital River Laboratory Animal Technology Co., China) using the EasySep™ Mouse CD8 + T Cell Separation Kit (19853_C, StemCell Technologies). The isolated CD8 + T cells were incubated with CD3-FITC antibody (11–0032-82, 1:50, ThermoFisher, USA) and CD8-APC antibody (47–0081-82, 1:50, ThermoFisher, USA), and their purity was confirmed by flow cytometry, showing > 97% CD8 + T cells.

CD8+ T cells were cultured in RPMI-1640 medium (R4130, Sigma, USA) and activated by adding CD3 antibody (2 μg/mL; 11–0032-82, 1:50, ThermoFisher, USA), CD28 antibody (1 μg/mL, 12–0281-82, ThermoFisher, USA), and interleukin-2 (IL-2, 5 ng/mL; 402-ML-100/CF, R&D Systems, USA).

Activated CD8+ T cells were then treated with PBS, RT + IT exo (5 μg/mL), sh-NC + RT + IT exo (5 μg/mL), or sh-PTEN + RT + IT exo (5 μg/mL) for 24 h before T cells being harvested for analysis.

Flow cytometry phenotype analysis

Single-cell suspensions from various cell groups or mouse tumor tissues were prepared for flow cytometry phenotype analysis. For T cell analysis, cells were stained with antibodies against PE-CD8 (12-0081-82, 1:50, ThermoFisher, USA), FITC-CD45 (11-0451-82, 1:50, ThermoFisher, USA), FITC-Ki67 (11-5698-82, 1:50, ThermoFisher, USA), eFluor™ 450-IFN-γ (48-7311-82, 1:50, ThermoFisher, USA), and FITC-Granzyme B (11-8898-82, 1:50, ThermoFisher, USA). The proportion of CD8+ T cells, Ki67+CD8+ T cells, IFN-γ+Granzyme B+CD8+ T cells, Granzyme B+CD8+ T cells, and IFN-γ+CD8+ T cells were analyzed using a FACSCalibur flow cytometer (BD Biosciences, USA) and CellQuest Pro software (BD Biosciences, USA).

For macrophage analysis, cells were stained with antibodies against PE-CD206 (12-2069-42, 1:50, ThermoFisher, USA) and FITC-CD86 (MHCD8601, 1:50, ThermoFisher, USA). Flow cytometry was performed using a FACSCalibur flow cytometer (BD Biosciences, USA), and data were analyzed using CellQuest Pro software (BD Biosciences, San Jose, CA, USA).

ELISA

Cell supernatants from each group were collected and analyzed using ELISA kits according to the manufacturer's instructions for Granzyme B (ab238265, Abcam, UK) and INF-γ (ab100689, Abcam, UK).

Statistical analysis

All data were processed using SPSS 22.0 (SPSS, Inc., Chicago, IL, USA) and GraphPad Prism 9.5 software. Quantitative data were expressed as mean ± standard deviation (SD). Comparisons between two groups were performed using an unpaired t-test, while comparisons among multiple groups were conducted using a one-way analysis of variance (ANOVA). The homogeneity of variance was tested using Levene's test. When variances were equal, Dunnett's t and LSD-t tests were used for pairwise comparisons. When variances were unequal, Dunnett's T3 test was used. A p-value < 0.05 was considered statistically significant.

Results

Preparation and characterization of serum exos from patients

Nasopharyngeal carcinoma (NPC) treatment faces challenges, as cancer cells can evade immune detection, reducing the effectiveness of immunotherapy. More biomarkers are needed to predict treatment outcomes and monitor progress. Exosomes, which carry proteins and RNA, play a key role in communication between cells and could serve as biomarkers for disease monitoring and therapy assessment. These exosomal proteins regulate tumor growth, immune response, and metastasis, making them valuable for cancer diagnosis and treatment [40–42].

This study utilizes advanced nanofluidic technology and machine learning methods to screen key protein biomarkers from exosomes of nasopharyngeal carcinoma (NPC) patients that can predict the efficacy of radiotherapy combined with immunotherapy (RT + IT). By systematically collecting and analyzing exosomes from patients before and after treatment, the study will explore and compare the dynamic changes of exosomal proteins and mRNA before and after NPC treatment and their correlation with treatment outcomes. Initially, exosomes were extracted from the serum of NPC patients and RT + IT-treated NPC patients (NPC exo, RT + IT-NPC exo). TEM revealed heterogeneous lipid bilayer vesicles with approximately 30–100 nm diameters, exhibiting cup-shaped or irregular morphologies (Fig. 1A). WB results showed that both exo types were highly enriched in exosomal markers CD63, CD81, and Alix, with minimal expression of Calnexin (Fig. 1B). NTA indicated that the diameters of both exo types ranged from 30 to 100 nm (Fig. 1C). To further investigate the uptake of NPC exo and RT + IT-NPC exo by NPC cells, we labeled NPC exo and RT + IT-NPC exo with Cy5.5 and co-incubated them with C666-1 cells. Fluorescence microscopy revealed that both NPC exo and RT + IT-NPC exo were internalized by C666-1 cells (Fig. 1D). To confirm the in vivo tumor-targeting ability of NPC exo and RT + IT-NPC exo, we intravenously injected Cy5.5-labeled exos into mice with subcutaneous tumors. In vitro fluorescence imaging showed that the fluorescence signals of NPC exo and RT + IT-NPC exo were primarily enriched in the tumors, liver, and lungs (Fig. 1E).

These results indicate that we successfully isolated NPC exo and RT + IT-NPC exo, which can recognize and target tumor cells.

Transcriptomic and proteomic screening of DEGs/DEPs

After successfully preparing and characterizing exos from NPC patients and post-RT + IT, we utilized transcriptomic sequencing and proteomic methods to investigate the differential expression in NPC exo and RT + IT-NPC exo. The study workflow is illustrated in Figure S1. We performed transcriptomic sequencing and proteomic analysis on NPC exo and RT + IT-NPC exo samples. Transcriptomic sequencing revealed 1,088 DEGs between NPC exo and RT + IT-NPC exo (Fig. 2A). A heatmap of the top 50 upregulated and downregulated genes, ranked by the degree of differential expression, was generated (Fig. 2B). Proteomic analysis identified 1,120 DEPs between the two exo types (Fig. 2C), and a heatmap of the top 50 upregulated and downregulated proteins was created (Fig. 2D).

Integrating transcriptomic and proteomic data, we analyzed the intersections of differentially expressed mRNAs and proteins between NPC exo and RT + IT-NPC exo. The Venn diagram identified 60 commonly expressed genes/proteins (Fig. 2E). A radar plot was created based on the log2 fold change (log2FC) of these genes/proteins, displaying their quadrant information (Fig. 2F).

(See figure on next page.)

Fig. 1 Preparation and characterization of NPC exo and RT + IT-NPC exo. **A** TEM observation of the morphological characteristics of NPC exo and RT + IT-NPC exo (scale bar = 100 nm); **B** WB analysis for the expression of CD63, CD81, Calnexin, and Alix in NPC exo and RT + IT-NPC exo; **C** NTA to assess the particle size distribution of NPC exo and RT + IT-NPC exo; **D** Immunofluorescence detection of C666-1 cells' uptake of Cy5.5-labeled exos (scale bar = 25 μm), with Cy5.5 marking NPC exo and RT + IT-NPC exo in red, and DAPI staining the nuclei in blue; **E** In vivo fluorescence imaging to track the biodistribution of exos in major organs and tumors across groups. Cell experiments were repeated three times, and each mouse group consisted of six individuals

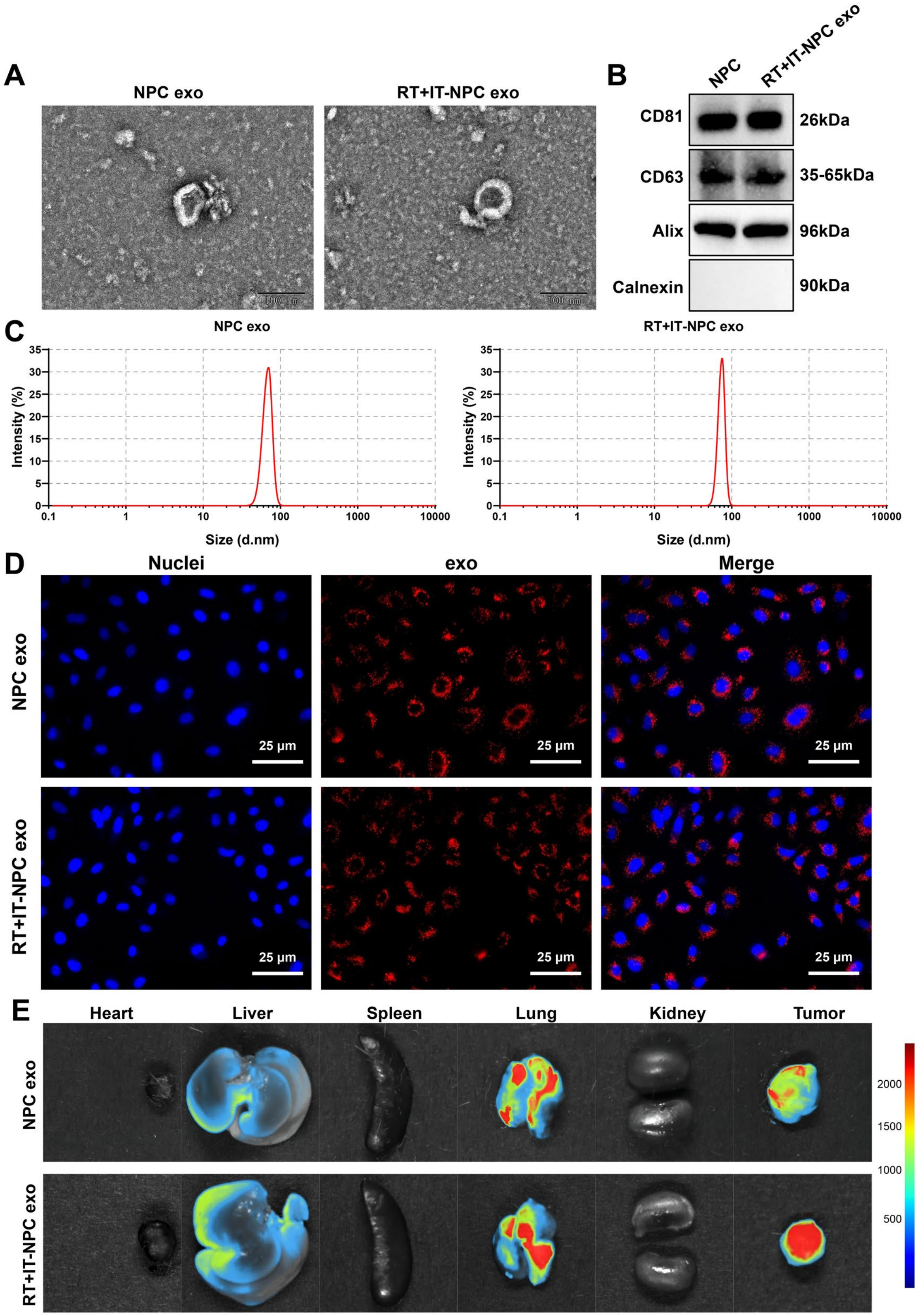

Fig. 1 (See legend on previous page.)

Our integrated transcriptomic and proteomic data analysis revealed significant differences between NPC exo and RT + IT-NPC exo samples. The 60 commonly expressed genes/proteins may play crucial roles in the efficacy of RT + IT for NPC.

Machine learning analysis to identify exosomal proteins predictive of RT + IT NPC efficacy

We applied two machine learning algorithms to screen the 60 intersecting DEGs/DEPs: LASSO regression and SVM-RFE. These two methods are effective in handling high-dimensional data, enabling efficient variable selection and regularization to avoid overfitting and enhance model prediction accuracy and interpretability. In the LASSO regression model, the Lambda parameter was optimized through cross-validation to minimize error, identifying three key genes (Fig. 3A). Using the "svmRadial" method, the SVM-RFE algorithm identified 31 key genes (Fig. 3B). The intersection of genes identified by both algorithms, represented in a Venn diagram, revealed a single feature gene: PTEN (Fig. 3C). To enhance the robustness of the model, sequencing results from repeat samples were used as training data. Although this may affect sample independence, repeated sequencing helps reduce random errors and improve data reliability. This strategy provided sufficient information for model training, facilitating a better understanding of the complex patterns in the data.

To further validate the feature gene's diagnostic capability and expression level, ROC curve analysis showed that PTEN, identified through machine learning, possesses strong diagnostic and predictive power, with an AUC value of 1 (Fig. 3D). PTEN expression was significantly upregulated in the RT + IT-NPC exo group compared to the NPC exo group, consistent with the proteomic expression trend (Fig. 3E, F).

These results indicate that PTEN, identified through machine learning, is a key biomarker for predicting the efficacy of RT + IT in NPC. Its expression level is significantly elevated in exos from NPC cells undergoing RT + IT.

Increased PTEN expression in NPC patients following RT + IT

To further verify the expression levels of PTEN in IR + RT NPC, we assessed its expression in NPC and IR + RT NPC tissues using immunohistochemistry, RT-qPCR, and WB. PTEN expression significantly increased in IR + RT NPC tissues compared to NPC tissues (Figure S2A-C). These findings indicate a significant elevation in PTEN expression in tissues of NPC patients following IR + RT.

Preparation and characterization of cell-derived exos

In the preliminary bioinformatics analysis, this study utilized exos derived from patients to screen for potential biomarkers. To further investigate and validate the function of the key protein PTEN within exos, cell-derived exos were used in subsequent experiments.

We employed a sh-PTEN lentivirus to infect C666-1 cells and harvested sh-PTEN + RT + IT exos post-RT + IT, selecting the most effective shRNA sequence for further use (Figure S3A-B).

Exos were isolated from the supernatants of C666-1 cells post radiotherapy and immunotherapy, both transfected with sh-NC lentivirus and sh-PTEN lentivirus (RT + IT exo, sh-NC + RT + IT exo, sh-PTEN + RT + IT exo). TEM revealed these as heterogeneous lipid bilayer vesicles characterized by cup-shaped or irregular morphologies (Figure S4A). WB results showed that exos were highly enriched in exosomal markers CD63, CD81, and Alix, while

(See figure on next page.)

Fig. 2 Intersection of DEGs/DEPs in NPC exo and RT + IT-NPC exo samples identified through transcriptomic and proteomic analysis. **A** Volcano plots of DEGs from transcriptomic sequencing data in NPC exo and RT + IT-NPC exo groups (NPC exo group = 3, RT + IT-NPC exo group = 3). Red dots represent significantly upregulated genes, blue dots represent significantly downregulated genes, and black dots indicate no differential expression. **B** Heatmap of the top 50 most significantly upregulated and downregulated genes from transcriptomic sequencing data, with red indicating high expression and blue indicating low expression. **C** Volcano plots of DEGs from proteomic sequencing data in NPC exo and RT + IT-NPC exo groups (NPC exo group = 6, RT + IT-NPC exo group = 6). Red dots signify significantly upregulated genes, blue dots signify significantly downregulated genes, and black dots show no expression difference. **D** Heatmap of the top 50 most significantly upregulated and downregulated genes from proteomic sequencing data, with red representing high expression and blue representing low expression. **E** Venn diagram showing the intersection of DEGs from transcriptomic sequencing data and DEPs from proteomic sequencing data. **F** Analysis of the correlation between log2FC of intersecting DEGs/DEPs from transcriptomic and proteomic datasets. Quadrants 1 and 9: mRNA and corresponding proteins are inconsistent, indicating post-transcriptional or post-translational regulation, such as miRNA targeting genes. Quadrants 2 and 8: mRNA expression differences with no corresponding protein change, suggesting post-transcriptional or translational-level regulation. Quadrants 3 and 7: mRNA and corresponding proteins show the same pattern of expression differences, indicating simultaneous transcriptional and translational changes. Quadrants 4 and 6: Protein expression differences with no corresponding mRNA changes, potentially due to translational regulation or protein accumulation. Quadrant 5: Co-expressed mRNA/proteins do not show differential expression; most genes and proteins show no differential expression

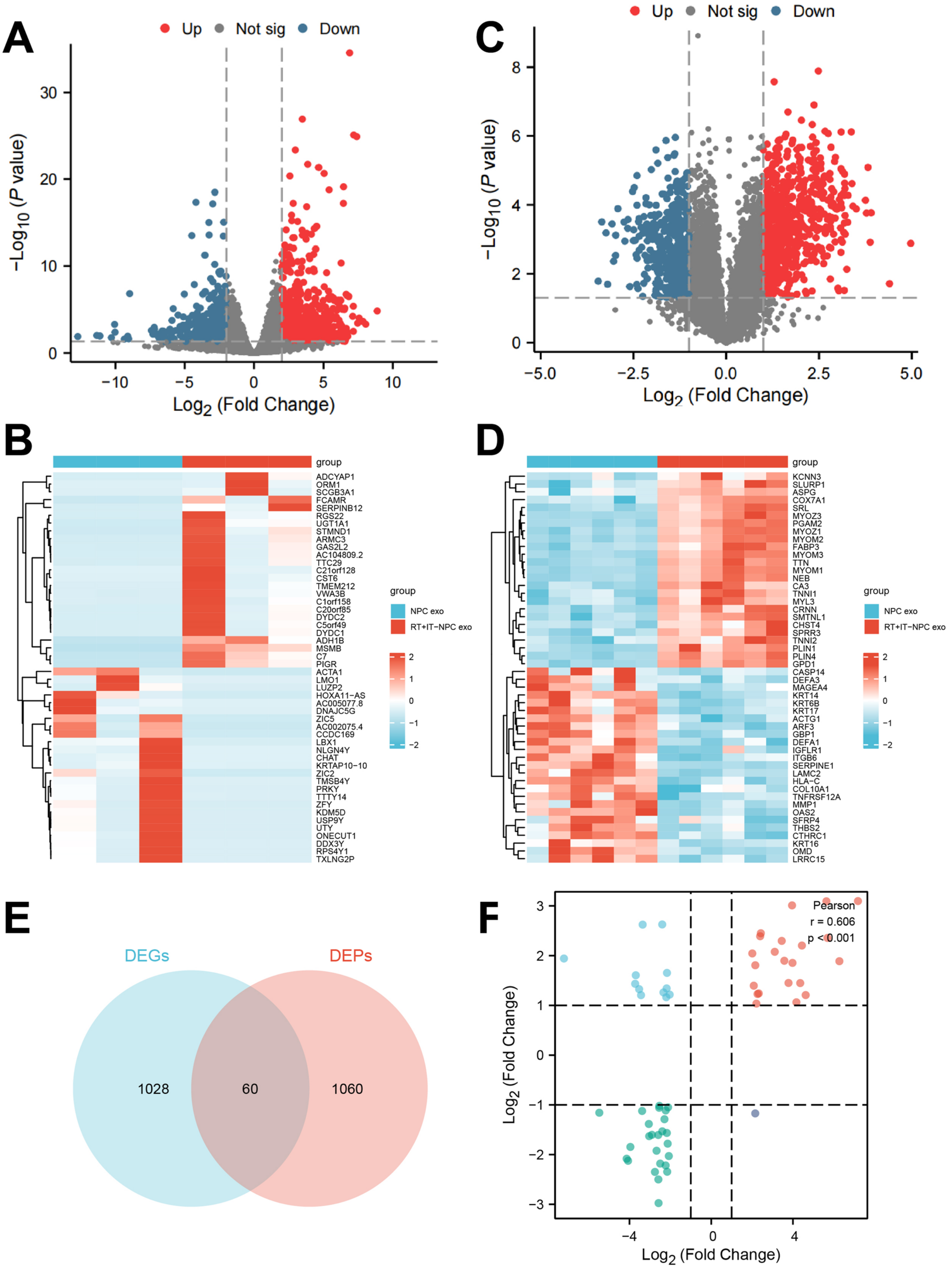

Fig. 2 (See legend on previous page.)

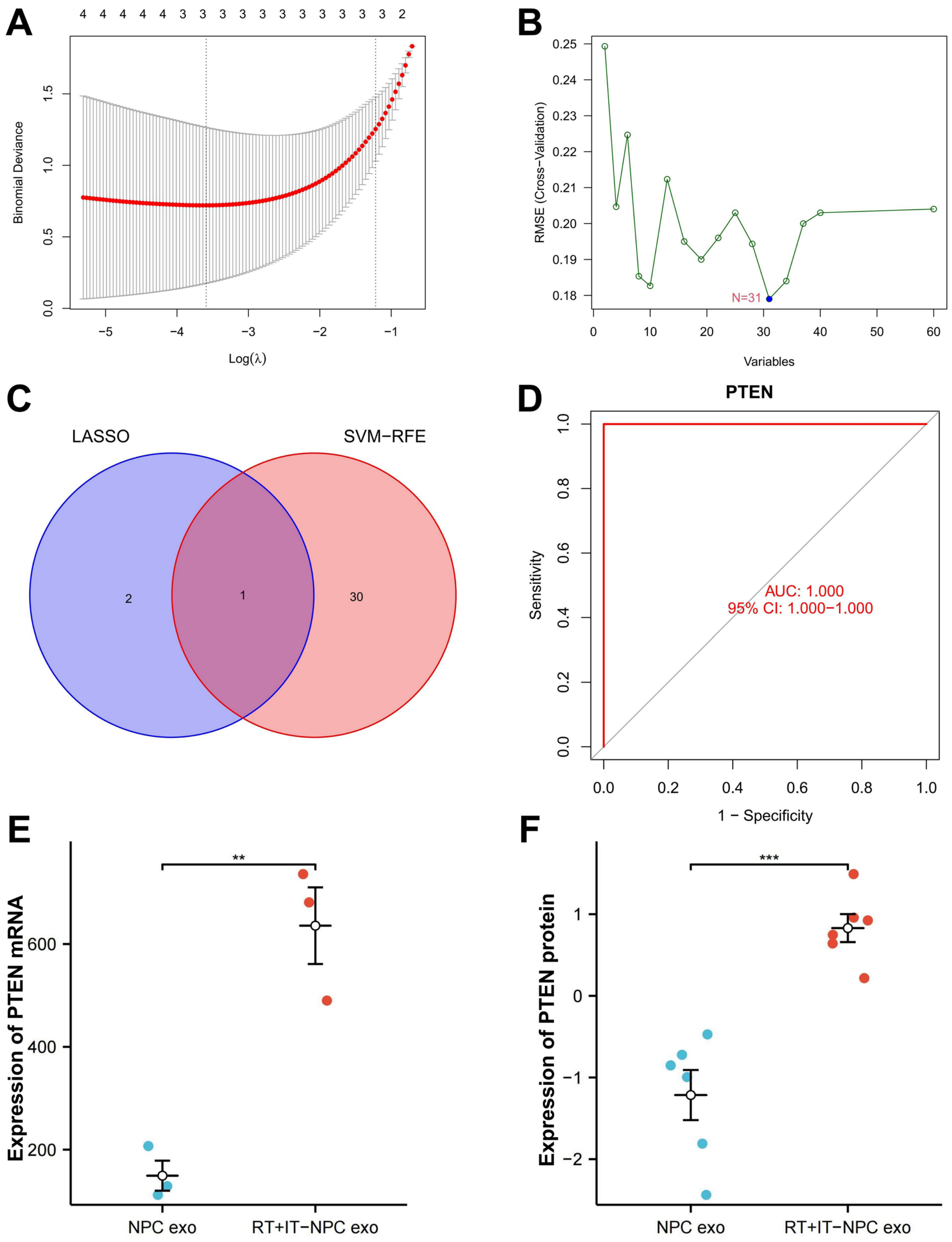

Fig. 3 Selection and validation of feature genes. **A** The LASSO algorithm identified 3 feature genes. **B** The SVM-RFE algorithm identified 31 feature genes. **C** Venn diagram showing the intersection of results from two machine learning algorithms, yielding 1 common gene. **D** ROC curve of PTEN in the sequencing dataset. **E** Expression of PTEN in transcriptomic sequencing data (NPC exo group = 3, RT + IT-NPC exo group = 3). **F** Expression of PTEN in proteomic sequencing data (NPC exo group = 6, RT + IT-NPC exo group = 6). $^{**}p < 0.01$, $^{***}p < 0.001$

Calnexin was barely expressed. Additionally, we confirmed that the exos used in the tumor implantation mouse model exhibited significantly reduced PTEN expression in the sh-PTEN + RT + IT exo group (Figure S4B). NTA indicated that the diameter of these exos ranged from 30–200 nm (Figure S4C).

To further investigate the uptake of RT + IT exo, sh-NC + RT + IT exo, and sh-PTEN + RT + IT exo by NPC cells, we incubated C666-1 cells with these exos labeled with Cy5.5 for 1 h. Fluorescence microscopy revealed that all exo variants were internalized by C666-1 cells (Figure S4D). To validate the in vivo tumor-targeting capabilities of these exos, we intravenously injected Cy5.5-labeled exos into mice bearing subcutaneous xenografts. In vitro fluorescence imaging demonstrated that the signals from RT + IT exo, sh-NC + RT + IT exo, and sh-PTEN + RT + IT exo were predominantly localized in the tumor, liver, and lungs (Figure S4E).

Additionally, H&E staining indicated that the major organs of the mice (including the heart, liver, spleen, lungs, and kidneys) exhibited normal histological structures (Figure S4F). This suggests that the three types of exos do not adversely affect the function of these organs, indicating good biocompatibility.

Impact of PTEN knockdown on the efficacy of exo-enhanced RT + IT in C666-1 cells

We conducted in vitro experiments to validate the role of exosomal protein PTEN in predicting the efficacy of RT + IT in NPC. Flow cytometry, EdU incorporation, and colony formation assays were used to assess apoptosis and proliferation. Results indicated that cells treated with RT + IT exhibited increased apoptosis and reduced proliferation compared to the control group. Cells treated with RT + IT exo showed further increases in apoptosis and decreased proliferation. Knocking down PTEN led to decreased apoptosis and increased proliferation compared to the RT + IT + sh-NC + RT + IT exo group (Fig. 4A–C).

Wound healing and Transwell assays demonstrated that compared to the control group, the invasive and migratory capabilities of cells were reduced after RT + IT. These capabilities were further diminished following treatment with RT + IT exo. However, knocking down PTEN enhanced invasion and migration capabilities compared to the group treated with RT + IT + sh-NC + RT + IT exo (Fig. 4D, E).

These findings suggest that knocking down PTEN counteracts the therapeutic effects of exos in enhancing the efficacy of RT + IT in C666-1 cells.

Impact of PTEN knockdown on exo efficacy in RT + IT in subcutaneous tumor models

To further investigate the role of exosomal protein PTEN in predicting the efficacy of RT + IT in NPC, tumor growth was assessed through tumor weight measurements and growth curves. Compared to the control group, tumors in the RT + IT group showed reduced growth rates and weights. Treatment with RT + IT exo further decreased growth rate and tumor weight compared to the RT + IT group. However, the knockdown of PTEN resulted in increased tumor growth rates and weights compared to the RT + IT + sh-NC + RT + IT exo group (Fig. 5A, B).

H&E staining revealed that compared to the control group, post-RT + IT tumors had reduced inflammatory cell infiltration, tighter cellular arrangement, more normalized cell morphology, more uniform nuclei, and visible nucleoli. These improvements were more pronounced after RT + IT exo treatment. In contrast, PTEN knockdown increased inflammatory cell infiltration, looser cellular arrangement, abnormal cell morphology, uneven nuclear sizes, and indistinct nucleoli compared to the RT + IT + sh-NC + RT + IT exo group (Fig. 5C).

Ki67 immunohistochemical staining results indicated a significant reduction in Ki67 expression following RT + IT compared to the control group. This reduction was even more significant after RT + IT exo treatment. Conversely, PTEN knockdown significantly increased Ki67 expression compared to the RT + IT + sh-NC + RT + IT exo group (Fig. 5D).

These findings suggest that knocking down exosomal protein PTEN inhibits the efficacy of exos in enhancing the outcome of RT + IT in NPC mouse models.

Knockdown of PTEN promotes M2 macrophage polarization and inhibits T cell proliferation

M2 macrophages play an important role in tumor development [43, 44]. In NPC, the accumulation of M2-type macrophages is closely associated with tumor growth, invasion, and poor prognosis. These cells support tumor immune escape within the tumor microenvironment by promoting tumor cell proliferation, invasion, and anti-apoptotic capabilities and by producing immunosuppressive factors [45, 46]. Therapeutic strategies in NPC, such as the use of RT + IT, can alter macrophage composition and functional states within the tumor microenvironment. Therefore, targeting the polarization and function of macrophages can significantly impact the therapeutic outcomes in NPC, offering a vital perspective for developing new treatment strategies. Recent studies have also highlighted PTEN's crucial role in macrophage

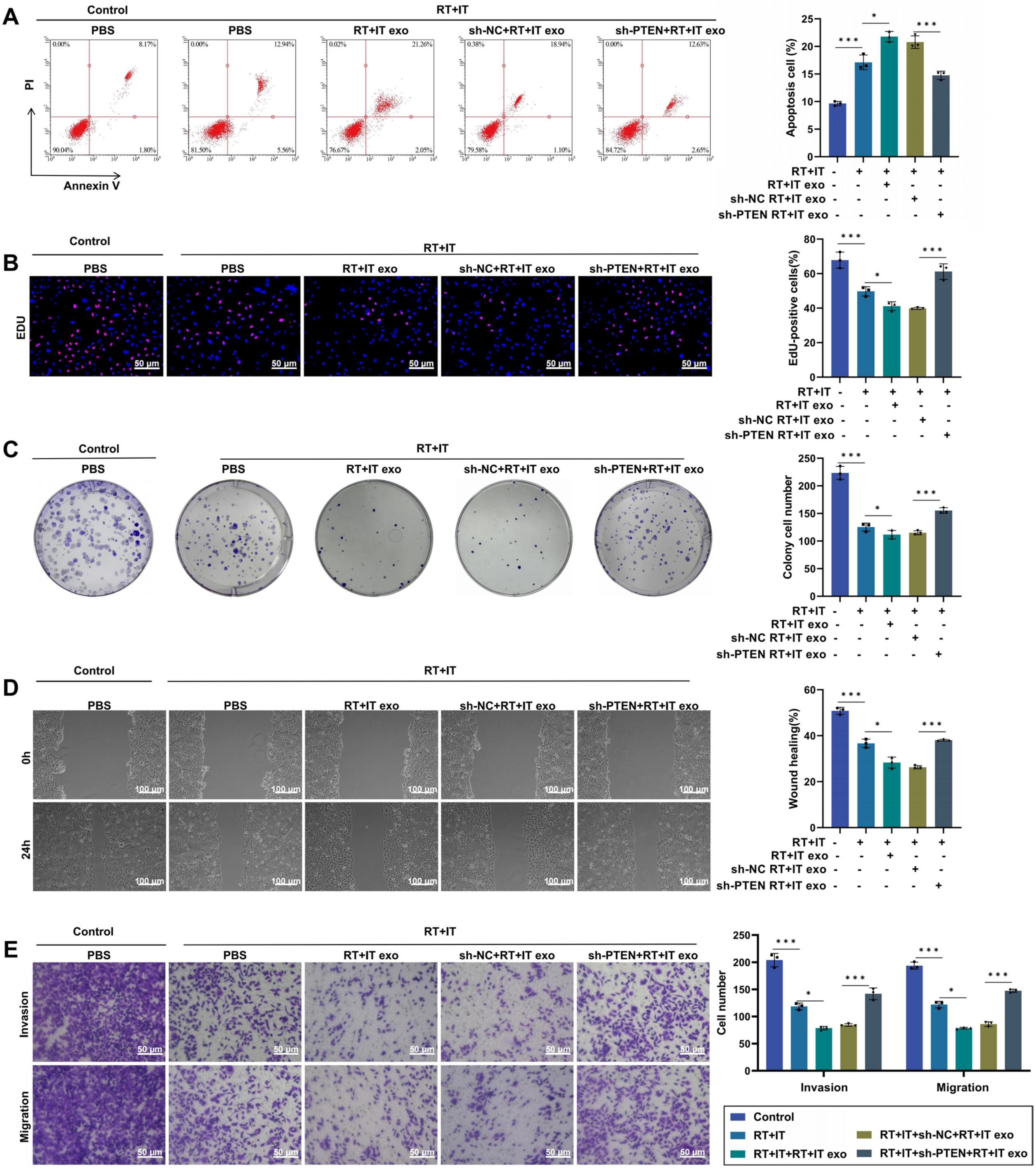

Fig. 4 Impact of PTEN knockdown on the efficacy of RT + IT in C666-1 cells. **A** Flow cytometry analysis of apoptosis in each group. **B** EdU assay to assess cell proliferation capabilities (red fluorescence indicates proliferating cells, with DAPI staining nuclei in blue) (scale bar: 50 μm). **C** Colony formation assay to evaluate the colony-forming ability of cells in each group. **D** Wound healing assay to measure cell migration ability in each group. **E** Transwell assay to assess cell invasion and migration capabilities (scale bar = 50 μm). *$p < 0.05$, ***$p < 0.001$. All cell experiments were repeated three times

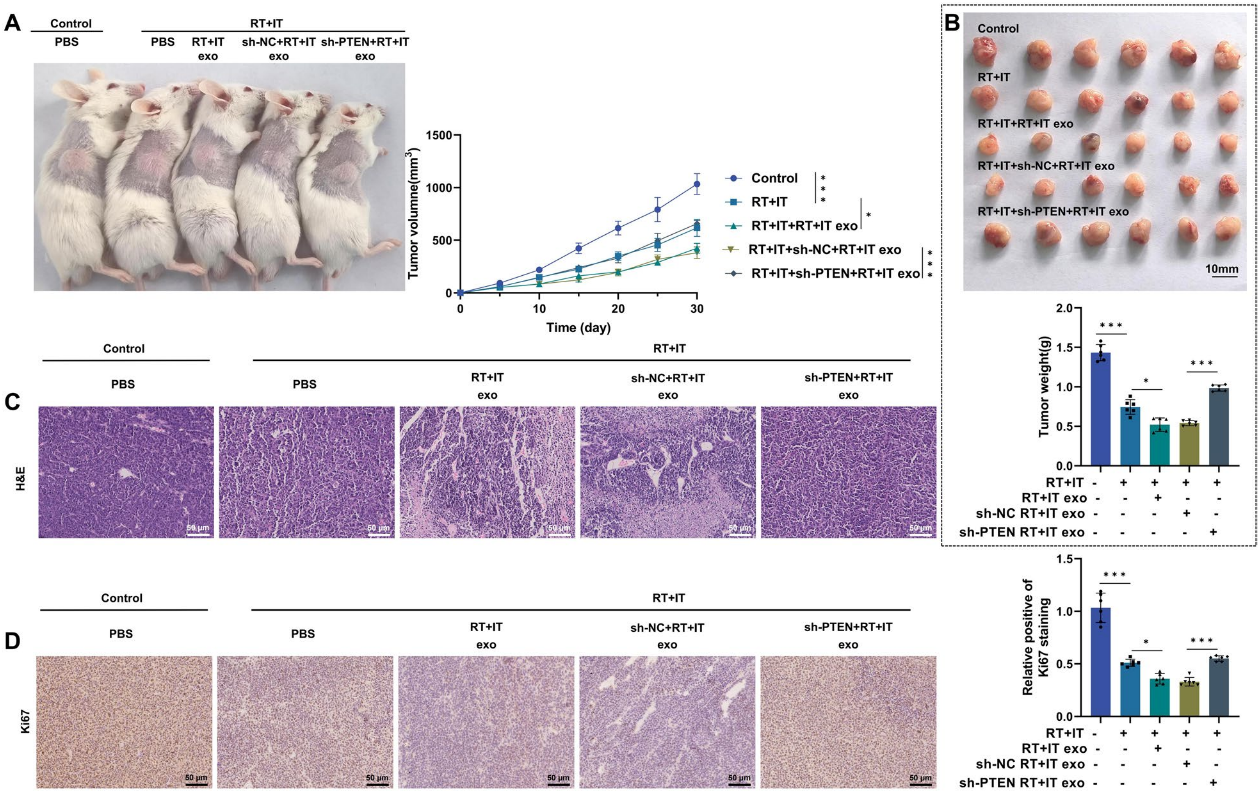

Fig. 5 Effect of PTEN knockdown on the efficacy of RT + IT in subcutaneous xenograft mice. **A** Tumor growth curves for each mouse group. **B** Tumor weights of each mouse group. **C** H&E staining images of tumors from each group (scale bar = 50 μm). **D** Immunohistochemical analysis of Ki67 expression in tumors from each mouse group (scale bar = 50 μm). Asterisks indicate statistical comparisons between groups, *$p < 0.05$, ***$p < 0.001$. Each group consisted of six mice

polarization and function, with overexpression of PTEN significantly inhibiting M2 macrophage polarization [47].

Subsequently, we explored the effects of knocking down exosomal PTEN on M2 macrophage polarization. IL-4 was used to differentiate M0 macrophages into M2 macrophages, and different groups of exos were co-cultured with M2 macrophages. Flow Cytometry results showed that compared to the control group, the M2 macrophage marker CD206 expression significantly increased after IL-4 induction. Following co-culture with RT + IT exo, there was a significant decrease in CD206 expression compared to the IL-4 group. Conversely, CD206 expression significantly increased after PTEN knockdown compared to the sh-NC + RT + IT exo group (Fig. 6A).

RT-qPCR and immunofluorescence assays demonstrated that post-IL-4 induction, expressions of M2 markers CD206, IL-10, and Arg-1 significantly increased compared to the control group. These expressions significantly decreased after co-cultivation with RT + IT exo compared to the IL-4 group; however, expressions significantly increased following PTEN knockdown compared to the sh-NC + RT + IT exo group (Fig. 6B, C).

These findings suggest that PTEN knockdown promotes polarization of M2 macrophages.

Effective infiltration of CD8+ T cells is closely associated with favorable prognoses in NPC, highlighting their critical role in suppressing tumor progression. Radiotherapy and immunotherapy strategies in NPC aim to activate the CD8+ T cell response to improve therapeutic outcomes. Radiotherapy enhances tumor cells' immunogenicity, promoting tumor antigens' presentation and activating CD8+ T cells. Therefore, optimizing the activity and functionality of CD8+ T cells and overcoming the immunosuppressive tumor microenvironment is crucial for enhancing treatment efficacy in NPC. Additionally, studies have shown that PTEN mRNA nanoparticles can reverse the immunosuppressive tumor microenvironment by promoting the infiltration of CD8+ T cells and enhancing the expression of pro-inflammatory cytokines [48].

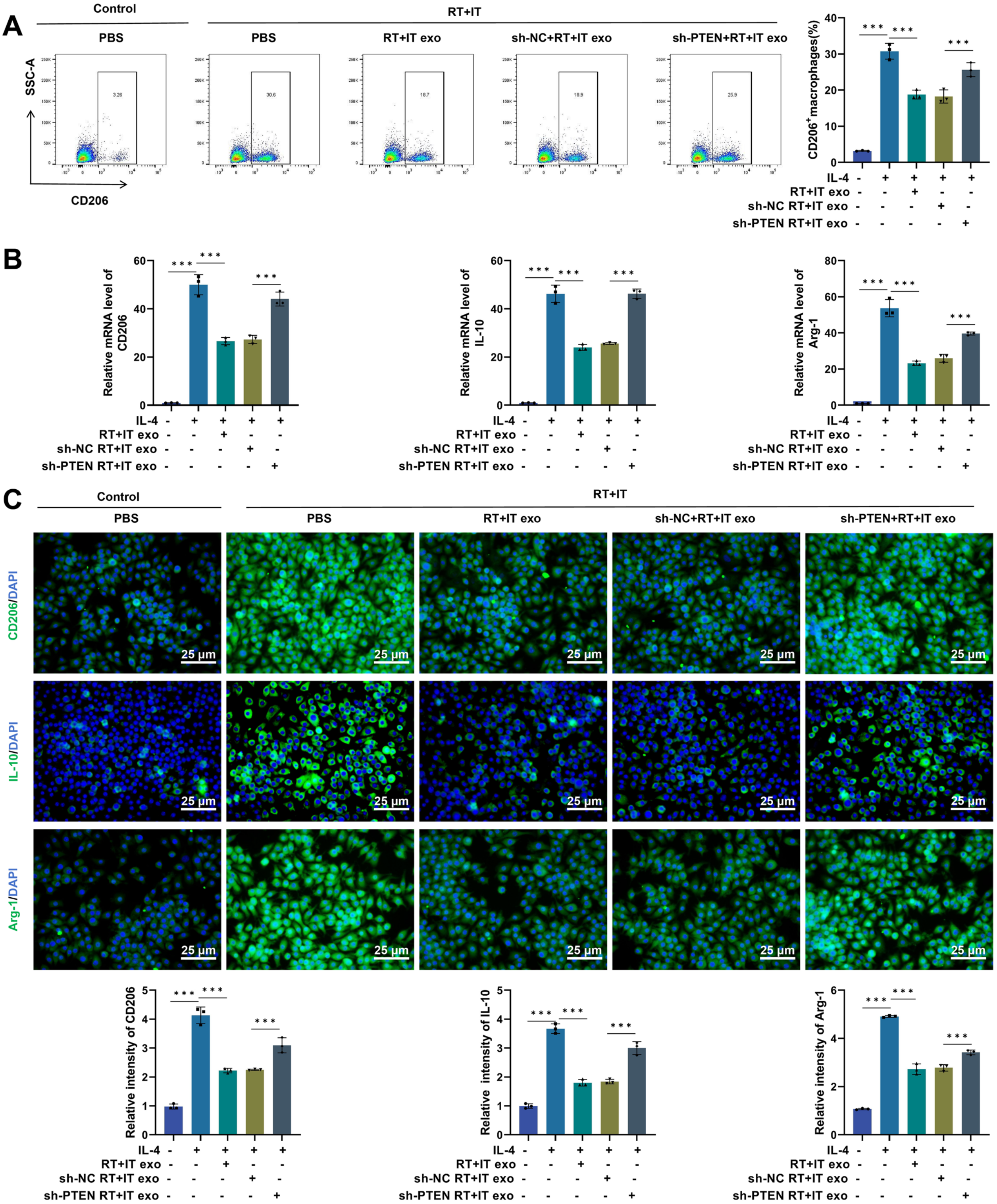

Fig. 6 Impact of PTEN knockdown on macrophages. **A** Flow cytometry analysis of CD206 expression in each cell group. **B** RT-PCR analysis of M2 macrophage markers CD206, IL-10, and Arg-1 mRNA expression in each cell group. **C** Immunofluorescence analysis of M2 macrophage markers CD206, IL-10, and Arg-1 expression in each cell group (scale bar = 25 μm). ***$p < 0.001$. All cell experiments were repeated three times

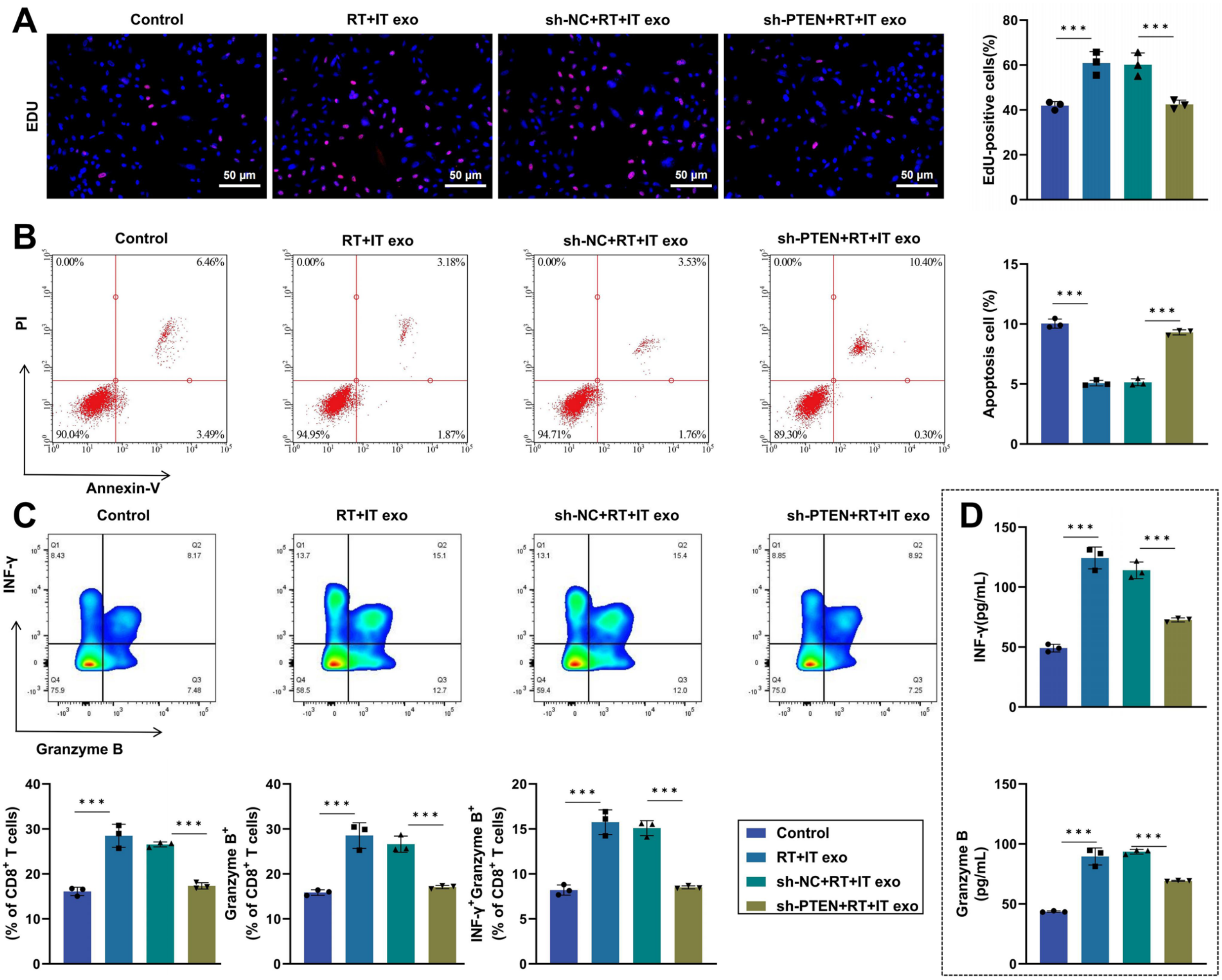

Fig. 7 Effects of PTEN knockdown on CD8+ T cells. **A** EdU assay to assess proliferation of CD8+ T cells in each group, with proliferating cells indicated by red fluorescence and nuclei marked by DAPI (blue) (scale bar = 50 μm). **B** Flow cytometry analysis of apoptosis in CD8+ T cells across different groups. **C** Flow cytometry analysis of the proportions of TNF-γ+Granzyme B+CD8+ T cells, TNF-γ+CD8+ T cells, and Granzyme B+CD8+ T cells in each group. **D** ELISA to measure TNF-γ and Granzyme B levels in cells from each group. ***$p < 0.001$. All cell experiments were repeated three times

We explored the effects of knocking down exosomal PTEN on CD8+ T cells. EdU incorporation and flow cytometry results indicated that the RT + IT exo group exhibited increased T cell proliferation and decreased apoptosis compared to the control group. However, knocking down PTEN reduced proliferation and increased apoptosis compared to the sh-NC + RT + IT exo group (Fig. 7A-B).

Flow cytometry analysis of T cell cytokines IFN-γ and Granzyme B expression and secretion showed that compared to the control group, RT + IT exo enhanced IFN-γ and Granzyme B expression and secretion in T cells. Conversely, PTEN knockdown reduced the expression and secretion of IFN-γ and Granzyme B compared to the sh-NC + RT + IT exo group (Fig. 7C, D).

These findings indicate that knocking down PTEN inhibits CD8+ T cell proliferation and function and promotes T cell apoptosis.

Remodeling of the immune microenvironment in subcutaneous tumor-bearing mice following PTEN knockdown-induced exo treatment with RT + IT

We explored the immunoregulatory effects of PTEN knockdown in an in vivo IR + RT NPC model. Flow cytometry and immunohistochemistry revealed that compared to the control group, the proportion of CD86+ macrophages increased, and CD206 + macrophages decreased following RT + IT. Treatment with RT + IT exo increased the proportion of CD86 + macrophages and decreased CD206+ macrophages compared to

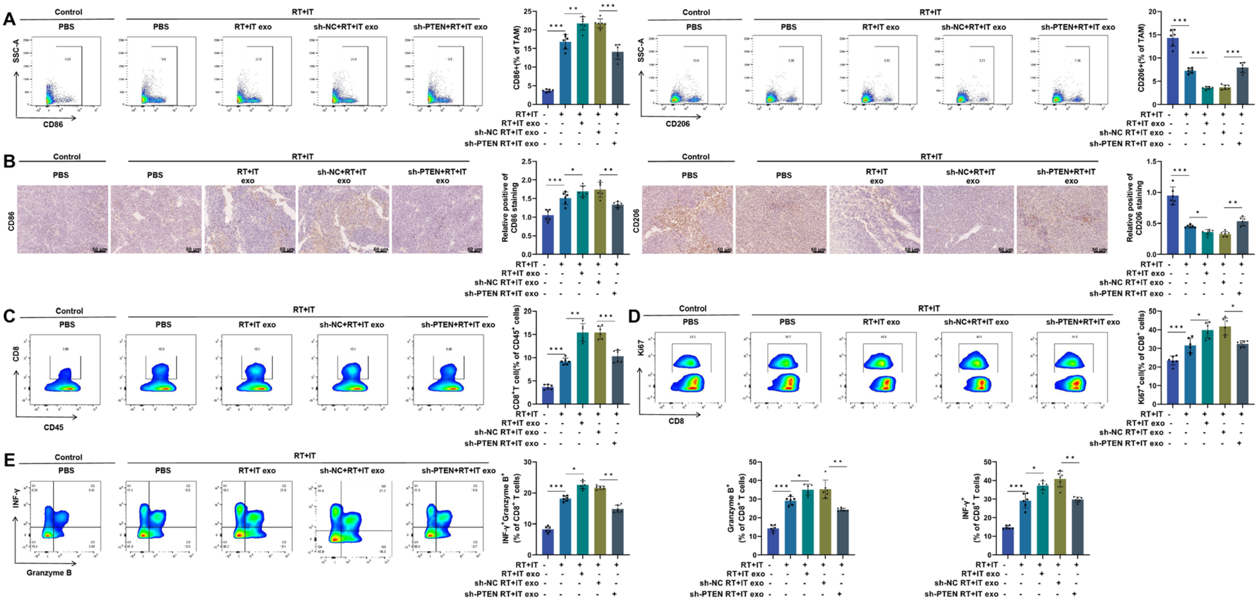

Fig. 8 PTEN knockdown effects on immune microenvironment macrophages and T cells. **A** Flow cytometry analysis of the ratio of M1 to M2 macrophages in each mouse group. **B** Immunohistochemistry to assess the expression of CD86 and CD206 in mice from each group (scale bar = 50 μm). **C** Flow cytometry analysis of the proportion of CD8+ T cells in each mouse group. **D** Flow cytometry analysis of the proportion of Ki67+CD8+ T cells in each mouse group. **E** Flow cytometry analysis of the proportions of IFN-γ+ Granzyme B+ CD8+ T cells, IFN-γ+ CD8+ T cells, and Granzyme B+ CD8+ T cells in each group. ***$p < 0.001$. Each group consisted of six mice

the RT + IT group. However, knocking down PTEN resulted in a decrease in CD86+ macrophages and an increase in CD206+ macrophages compared to the RT + IT + sh-NC + RT + IT exo group (Fig. 8A, B).

Flow cytometry also showed increases in the proportions of CD8+ T cells, KI67+ CD8+ T cells, IFN-γ+ Granzyme B+ CD8+ T cells, IFN-γ+ CD8+ T cells, and Granzyme B+ CD8+ T cells following rRT + IT compared to the control. These increases were more pronounced post-RT + IT exo treatment. In contrast, PTEN knockdown led to reductions in these cell populations compared to the RT + IT + sh-NC + RT + IT exo group (Fig. 8C, E), indicating that knocking down PTEN suppressed the content, proliferation, and function of CD8+ T cells.

These results demonstrate that PTEN knockdown induces significant remodeling of the immune microenvironment following RT + IT in subcutaneous tumor-bearing mice.

Discussion

NPC is a malignant tumor predominantly occurring in the nasopharynx, exhibiting significant geographical and ethnic variations in incidence rates globally, particularly prevalent in Southeast Asia and southern China [49, 50]. The treatment of NPC typically includes radiotherapy, chemotherapy, and immunotherapy. However, there are substantial individual differences in treatment outcomes, and the recurrence rate remains high [4–6]. Consequently, developing effective methods to predict treatment outcomes is crucial for providing more personalized treatment plans for patients [51]. In this context, our study explores nanofluidic technology combined with machine learning to screen and analyze exosomal proteins, specifically focusing on PTEN protein as a potential predictive biomarker for NPC treatment outcomes, aiming to enhance the selectivity and predictability of treatment.

This study employs nanofluidic technology and machine learning to predict the efficacy of RT + IT in NPC, representing a significant advancement beyond traditional biomarker research. Traditional methods typically rely on the expression levels of a single or a few biomarkers, whereas our approach allows for an integrated analysis across multiple data layers, enhancing the accuracy and reliability of predictions. Furthermore, nanofluidic technology significantly increases the quantity and quality of detectable exos from minimal sample volumes, improving experimental sensitivity and efficiency [52]. The introduction of machine learning further optimizes the data analysis process, enabling the extraction of useful information from complex biological data [53, 54]. The application of this integrated technology is relatively rare in previous studies, highlighting the innovative nature of our research.

Exos play a crucial role in intercellular communication and hold significant positions in cancer biomarker research [55–57]. In this study, the PTEN protein, a key tumor suppressor, is closely linked to the outcomes of radiotherapy and immunotherapy in NPC through its expression in exos. Unlike other studies, we not only focus on the quantity of PTEN expression but also investigate its forms and functional mechanisms within exos, which have been less explored in previous research [22, 58, 59]. Additionally, through machine learning analysis, we can predict its therapeutic role more accurately, a capability often lacking in traditional biomarker research.

Integrating nanofluidic technology and machine learning in this study provides a novel perspective for screening and analyzing tumor biomarkers. This technological synergy enhances the precision of sample processing and optimizes the data analysis process, enabling the handling of large datasets and the identification of potential biomarkers. Compared to previous studies reliant on single technologies, this research demonstrates the advantages of integrating multiple technologies, particularly in efficiently and accurately processing high-dimensional biological data. This level of integration is often challenging to achieve in other studies, showcasing the forward-looking nature and application potential of our methodology [60, 61].

In this study, the consistency between in vitro and in vivo experimental results validates our research methods' reliability and underscores the rigor of our experimental design. By knocking down PTEN protein, we have closely observed the specific role of exos in modulating the tumor microenvironment, particularly highlighting their critical influence on M2 macrophage polarization and CD8 + T cell activity. This finding is prominently featured in our research and aligns closely with existing literature. Interestingly, as shown in Fig. 1E, compared with the NPC exo group, the RT + IT-NPC exo group was more enriched in the tumor. Transcriptomic and proteomic analyses revealed significant differences between NPC exo and RT + IT-NPC exo samples. The 60 co-expressed genes/proteins may play a critical role in NPC combined radiotherapy and immunotherapy (Fig. 2). Therefore, in addition to PTEN, there may be other genes regulating Exo uptake by tumors, further influencing the effectiveness of radiotherapy and immunotherapy in NPC, although this still needs to be confirmed by further experiments. Our approach employs a more systematic experimental design and complex data analysis methods, comprehensively explaining PTEN's mechanisms in the tumor microenvironment. This depth of mechanistic study is relatively rare in existing literature, which typically focuses more on describing phenomena than exploring the detailed biological processes behind them [62–64].

The application of machine learning in this research significantly enhances the efficiency and accuracy of protein predictions, revolutionizing the screening of biomarkers. By constructing complex predictive models, we can accurately identify proteins closely related to the treatment efficacy of NPC from a vast biomarker database. The effectiveness of this method surpasses traditional biomarker screening approaches, which often show limitations in handling large datasets. Our study utilizes advanced algorithms to optimize the predictive models, significantly improving the models' accuracy and application scope. The introduction of this method provides robust technological support for personalized and precision medicine in cancer treatment, demonstrating the broad prospects and potential value of machine learning in biomedical research.

Although this study has achieved certain outcomes, it still has some limitations. For instance, the relatively small sample size may restrict the results' general applicability and statistical power. Future research should expand the sample size and attempt to validate our findings across diverse ethnic and geographical patient populations. Additionally, while this study primarily focused on the PTEN protein, future investigations could explore the predictive effects of a broader range of exosomal proteins and their combinations. Technologically, future studies could further optimize data analysis algorithms to enhance the generalizability of predictive models.

This research confirms that the exosomal protein PTEN can be an effective predictive biomarker for RT + IT in NPC. These findings enrich the field of tumor biomarkers and offer new strategies for treating NPC. PTEN enhances the effectiveness of Exos in radiotherapy and immunotherapy, especially in regulating M2 macrophage polarization and T cell proliferation. PTEN regulates the remodeling of the immune microenvironment, which may provide a new regulatory mechanism for combined radiotherapy and immunotherapy. These findings emphasize the importance of further studying the role of exosomal proteins in tumor therapy mechanisms and provide new insights for optimizing NPC treatment strategies. Particularly in immune microenvironment regulation, PTEN's role not only influences the biological behavior of tumor cells but also significantly affects the host immune response.

Scientifically, this study demonstrates the potential application of nanofluidic technology and machine learning in predicting treatment outcomes, fostering the intersection of biomedical engineering and clinical medicine. Clinically, by accurately predicting treatment responses,

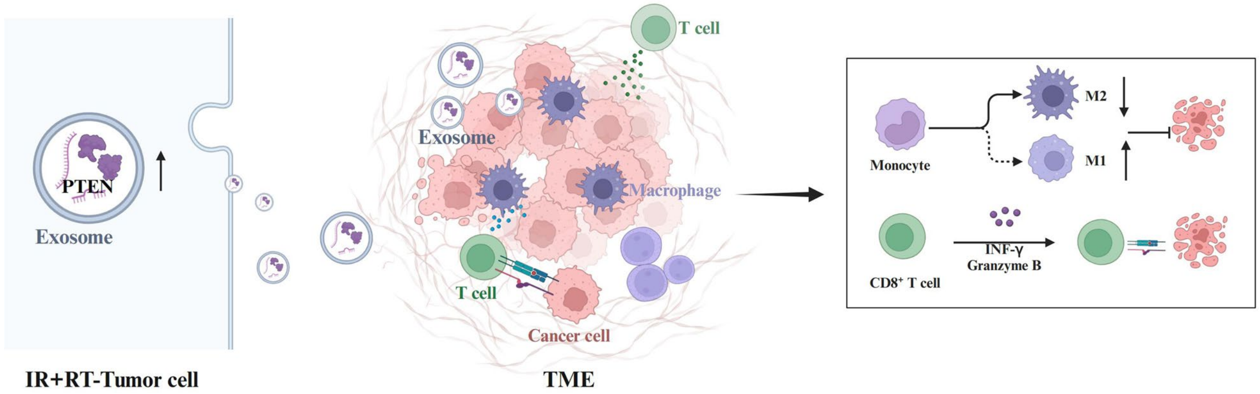

Fig. 9 Schematic of the molecular mechanism for predicting the efficacy of RT + IT in NPC using exosomal protein PTEN

more personalized treatment plans can be devised for patients, optimizing treatment efficacy, minimizing unnecessary side effects, and ultimately enhancing the quality of life for patients. Looking ahead, the outcomes of this study hold promise for further development and broader clinical application, potentially revolutionizing cancer treatment.

Conclusion

Based on the results, we can preliminarily conclude that Exosomal protein PTEN can be utilized to predict the efficacy of RT + IT in NPC (Fig. 9). In both in vitro and in vivo experiments, knocking down PTEN affected the influence of exos on the combined treatment, particularly in regulating M2 macrophage polarization and T cell proliferation. The knockdown of PTEN led to a remodeling of the immune microenvironment, potentially offering a new regulatory mechanism for RT + IT.

These findings underscore the importance of in-depth research into the mechanisms of exosomal proteins in cancer therapy, providing fresh insights for optimizing NPC treatment strategies. Notably, the role of PTEN extends beyond influencing the biological behaviors of tumor cells; it also significantly affects the host's immune response.

Despite the promising prospects of this study, there are several limitations. For instance, the study primarily relied on specific cell lines and mouse models, which may limit the general applicability of the findings. Moreover, while PTEN, identified through machine learning as a potential biomarker, holds promise, its clinical application still needs validation in larger-scale and multicenter clinical trials. Additionally, the safety and efficacy of exos as therapeutic vehicles also warrant further investigation in future studies.

In summary, this study reveals the potential role of PTEN in RT + IT for NPC and emphasizes the need for further research into exo-mediated cell communication in cancer treatment. Future research should focus on the detailed mechanisms of action of exosomal proteins and their potential for clinical application, thus providing more precise and effective treatment options for NPC patients.

Abbreviations

AUC	Area under the curve
ANOVA	Analysis of variance
DEGs	Differentially expressed genes
DEPs	Differentially expressed proteins
Exo	Exosome
ExoTENPO	Exo trajectory etching magnetic nanopore
FDR	False discovery rate
H&E	Hematoxylin and eosin
LASSO	Least absolute shrinkage and selection operator
NPC	Nasopharyngeal carcinoma
NTA	Nanoparticle tracking analysis
PTEN	Phosphatase and Tensin Homolog
ROC	Receiver operating characteristic
RT + IT	Radiotherapy combined with immunotherapy
SD	Standard deviation
SVM-RFE	Support vector machine-recursive feature elimination
TEM	Transmission electron microscopy
WB	Western blot

Supplementary Information

The online version contains supplementary material available at https://doi.org/10.1186/s12951-025-03315-z.

Supplementary Material 1. Figure S1. Research workflow diagram.

Supplementary Material 2. Figure S2. Expression of PTEN in IR + RT NPC. Note: (A) Immunohistochemistry analysis of PTEN expression in NPC tissue ($n = 6$) and IR + RT NPC tissue ($n = 6$) (scale bar = 100/50 μm). (B) RT-PCR analysis of PTEN expression in NPC and IR + RT NPC tissue. (C) WB analysis of PTEN expression in NPC and IR + RT NPC tissue.

Supplementary Material 3. Figure S3. Validation of PTEN knockdown efficiency. Note: (A-B) RT-PCR and WB analyses to evaluate the efficiency of PTEN knockdown in cells; $^{***}p < 0.001$. All cell experiments were repeated three times.

Supplementary Material 4. Figure S4. Characterization of RT + IT exo, sh-NC + RT + IT exo, and sh-PTEN + RT + IT exo. Note: (A) TEM observation of exosomal morphology in each group (scale bar = 100 nm). (B) WB analysis of CD63, CD81, Calnexin, Alix, and PTEN expression in exos from each group. (C) NTA of the particle size distribution of exos in each group. (D) Immunofluorescence detection of C666-1 cell uptake of Cy5.5-labeled exos from each group (scale bar = 25 μm), with Cy5.5 labeling RT + IT exo, sh-NC + RT + IT exo, and sh-PTEN + RT + IT exo (red) and DAPI staining nuclei (blue). (E) In vivo fluorescence imaging to assess the biodistribution of exos in major organs and tumors across groups. (F) Representative histological images of H&E staining sections of the heart, liver, kidney, spleen, and lungs from each mouse group (scale bar = 100 μm). All cell experiments were repeated three times, with six mice in each group.

Supplementary Material 5.

Acknowledgements
Not applicable.

Author contributions
Xiaoli Li was responsible for designing and conducting the exosome extraction, transcriptomic, and proteomic analyses, as well as performing in vitro experiments. Jiashuo Wang carried out the murine subcutaneous NPC model experiments and analyzed the immune microenvironment, including M2 macrophage polarization and CD8 + T cell activity. Ming Zhang supervised the overall study design, provided critical guidance for experimental workflows, and contributed to data interpretation. Jiaxing Guo performed data analysis, including the identification of treatment-related proteins, and assisted with manuscript preparation. All authors contributed to the manuscript's writing, revision, and approval of the final version for publication.

Funding
Not applicable.

Data availability
The datasets used or analyzed during the current study are available from the corresponding author on reasonable request.

Declarations

Ethics approval and consent to participate
Written informed consent was obtained from all participants, and the study was approved by Scientific Research Ethics Committee of China Medical University. All mouse experiments were conducted in accordance with institutional guidelines and approved by the Animal Care and Use Committee of China Medical University.

Consent for publication
Not applicable.

Competing interests
The authors declare no competing interests.

Author details
[1]Department of Otorhinolaryngology, The First Hospital of China Medical University, No.4, Chongshan Dong Road, Huanggu District, Shenyang 110001, China. [2]Department of Otorhinolaryngology, The 4th Affiliated Hospital of China Medical University, No. 155 Nanjing North Street, Heping District, Shenyang 110032, China.

Received: 27 September 2024 Accepted: 11 March 2025
Published: 21 April 2025

References

1. Wong KCW, Hui EP, Lo K-W, Lam WKJ, Johnson D, Li L, et al. Nasopharyngeal carcinoma: an evolving paradigm. Nat Rev Clin Oncol. 2021. https://doi.org/10.1038/s41571-021-00524-x.
2. Available from: http://jpp.krakow.pl/journal/archive/02_22/pdf/https://doi.org/10.26402/jpp.2022.1.12.pdf
3. King AD. MR imaging of nasopharyngeal carcinoma. Magn Reson Imaging Clin N Am. 2022. https://doi.org/10.1016/j.mric.2021.06.015.
4. Huang H, Yao Y, Deng X, Huang Z, Chen Y, Wang Z, et al. Immunotherapy for nasopharyngeal carcinoma: current status and prospects (review). Int J Oncol. 2023. https://doi.org/10.3892/ijo.2023.5545.
5. Morisaki T, Ohguri T, Yahara K, Nakahara S, Kakinouchi S, Itamura H, et al. Salvage re-irradiation with intensity-modulated radiotherapy, chemotherapy combined with hyperthermia for local recurrence of nasopharyngeal carcinoma after chemoradiotherapy. J UOEH. 2021. https://doi.org/10.7888/juoeh.43.355.
6. Zhu Q, Zhao G, Li Y, Talakatta G, Mai H, Le Q, et al. Advances in pathogenesis and precision medicine for nasopharyngeal carcinoma. MedComm. 2021. https://doi.org/10.1002/mco2.32.
7. Thamboo A, Patel VS, Hwang PH. 5-year outcomes of salvage endoscopic nasopharyngectomy for recurrent nasopharyngeal carcinoma. J Otolaryngol Head Neck Surg. 2021. https://doi.org/10.1186/s40463-020-00482-x.
8. El Korbi A, Ben Tkhayat S, Bouatay R, Ferjaoui M, Kolsi N, Harrathi K, et al. Résultats thérapeutiques des carcinomes nasopharyngés: étude monocentrique à l´hôpital universitaire Fattouma Bourguiba de Monastir en Tunisie. Pan Afr Med J. 2021. https://doi.org/10.11604/pamj.2021.38.143.15510.
9. Finazzi T, Rordorf T, Ikenberg K, Huber GF, Guckenberger M, Garcia Schueler HI. Radiotherapy-induced anti-tumor immune response and immune-related adverse events in a case of recurrent nasopharyngeal carcinoma undergoing anti-PD-1 immunotherapy. BMC Cancer. 2018. https://doi.org/10.1186/s12885-018-4295-8.
10. Baxevanis CN, Gritzapis AD, Voutsas IF, Batsaki P, Goulielmaki M, Adamaki M, et al. T-cell repertoire in tumor radiation: the emerging frontier as a radiotherapy biomarker. Cancers. 2022. https://doi.org/10.3390/cancers14112674.
11. Brites CDS, Marin R, Suta M, Carneiro Neto AN, Ximendes E, Jaque D, et al. Spotlight on luminescence thermometry: basics, challenges, and cutting-edge applications. Adv Mater. 2023. https://doi.org/10.1002/adma.202302749.
12. Tsutsui M, Takaai T, Yokota K, Kawai T, Washio T. Deep learning-enhanced nanopore sensing of single-nanoparticle translocation dynamics. Small Methods. 2021. https://doi.org/10.1002/smtd.202100191.
13. Sepehrnia M, Davoodabadi Farahani S, Hamidi Arani A, Taghavi A, Golmohammadi H. Laboratory investigation of GO-SA-MWCNTs ternary hybrid nanoparticles efficacy on dynamic viscosity and wear properties of oil (5W30) and modeling based on machine learning. Sci Rep. 2023. https://doi.org/10.1038/s41598-023-37623-x.
14. Chen X, Du Z, Huang M, Wang D, Fong WP, Liang J, et al. Circulating PD-L1 is associated with T cell infiltration and predicts prognosis in patients with CRLM following hepatic resection. Cancer Immunol Immunother. 2021. https://doi.org/10.1007/s00262-021-03021-3.
15. Peng M, Zhou Y, Zhang Y, Cong Y, Zhao M, Wang F, et al. Small extracellular vesicle CA1 as a promising diagnostic biomarker for nasopharyngeal carcinoma. Int J Biol Macromol. 2024. https://doi.org/10.1016/j.ijbiomac.2024.133403.
16. Liu J, Duan G, Yang W, Zhang S, Liu F, Peng Y, et al. Identification of transcription factors related to diabetic tubulointerstitial injury. J Transl Med. 2023. https://doi.org/10.1186/s12967-023-04069-8.
17. Liu W, Huang Y, Li Z, Li L, Zhao Y, Li M. Multivalent engineering of exosomes with activatable aptamer probes for specific regulation and monitoring of cell targeting. Anal Chem. 2022. https://doi.org/10.1021/acs.analchem.1c04741.
18. Valverde A, Seal A, Nares S, Shukla D, Naqvi AR. Human herpesvirus-encoded MicroRNA in host-pathogen interaction. Adv Biol Regul. 2021. https://doi.org/10.1016/j.jbior.2021.100829.
19. Wang YM, Peng ZY, Zhang LY, Wang YX, Fan RH, Zhang H, et al. N6-Methyladenosine RNA modification landscape in the occurrence and recurrence of nasopharyngeal carcinoma. World J Oncol. 2022. https://doi.org/10.14740/wjon1491.
20. Wang J, Liu Y, Zhang Y, Li X, Fang M, Qian D. Targeting exosomes enveloped EBV-miR-BART1-5p-antagomiRs for NPC therapy through both anti-vasculogenic mimicry and anti-angiogenesis. Cancer Med. 2023. https://doi.org/10.1002/cam4.5941.
21. Shi L, Zhu W, Huang Y, Zhuo L, Wang S, Chen S, et al. Cancer-associated fibroblast-derived exosomal microRNA-20a suppresses the PTEN/PI3K-AKT pathway to promote the progression and chemoresistance of

non-small cell lung cancer. Clin Transl Med. 2022. https://doi.org/10.1002/ctm2.989.
22. Jiang T-Y, Shi Y-Y, Cui X-W, Pan Y-F, Lin Y-K, Feng X-F, et al. PTEN deficiency facilitates exosome secretion and metastasis in cholangiocarcinoma by impairing TFEB-mediated lysosome biogenesis. Gastroenterology. 2023. https://doi.org/10.1053/j.gastro.2022.11.025.
23. Cao W, Zeng Z, He Z, Lei S. Hypoxic pancreatic stellate cell-derived exosomal mirnas promote proliferation and invasion of pancreatic cancer through the PTEN/AKT pathway. Aging. 2021. https://doi.org/10.18632/aging.202569.
24. Zhang M, Johnson-Stephenson TK, Wang W, Wang Y, Li J, Li L, et al. Mesenchymal stem cell-derived exosome-educated macrophages alleviate systemic lupus erythematosus by promoting efferocytosis and recruitment of IL-17+ regulatory T cell. Stem Cell Res Ther. 2022. https://doi.org/10.1186/s13287-022-03174-7.
25. Cheng H-Y, Hsieh C-H, Lin P-H, Chen Y-T, Hsu DS-S, Tai S-K, et al. Snail-regulated exosomal microRNA-21 suppresses NLRP3 inflammasome activity to enhance cisplatin resistance. J Immunother Cancer. 2022. https://doi.org/10.1136/jitc-2022-004832.
26. Wang S, Zhang MJ, Wu ZZ, Zhu SW, Wan SC, Zhang BX, et al. GSDME is related to prognosis and response to chemotherapy in oral cancer. J Dent Res. 2022. https://doi.org/10.1177/00220345211073072.
27. Santos-Otte P, Leysen H, van Gastel J, Hendrickx JO, Martin B, Maudsley S. G protein-coupled receptor systems and their role in cellular senescence. Comput Struct Biotechnol J. 2019. https://doi.org/10.1016/j.csbj.2019.08.005.
28. Bortoluzzi S, Lovisa F, Gaffo E, Mussolin L. Small RNAs in circulating exosomes of cancer patients: a minireview. High-Throughput. 2017. https://doi.org/10.3390/ht6040013.
29. Kwak G, Cheng J, Kim H, Song S, Lee SJ, Yang Y, et al. Sustained exosome-guided macrophage polarization using hydrolytically degradable PEG hydrogels for cutaneous wound healing: identification of key proteins and MiRNAs, and sustained release formulation. Small. 2022. https://doi.org/10.1002/smll.202200060.
30. Rao D, Lu H, Wang X, Lai Z, Zhang J, Tang Z. Tissue-derived exosome proteomics identifies promising diagnostic biomarkers for esophageal cancer. Elife. 2023. https://doi.org/10.7554/elife.86209.
31. Qi B, Kong L, Lai X, Wang L, Liu F, Ji W, et al. Plasma exosome proteomics reveals the pathogenesis mechanism of post-stroke cognitive impairment. Aging. 2023. https://doi.org/10.18632/aging.204738.
32. Li F, Xu T, Chen P, Sun R, Li C, Zhao X, et al. Platelet-derived extracellular vesicles inhibit ferroptosis and promote distant metastasis of nasopharyngeal carcinoma by upregulating ITGB3. Int J Biol Sci. 2022. https://doi.org/10.7150/ijbs.76162.
33. Liu Y, Wen J, Huang W. Exosomes in nasopharyngeal carcinoma. Clin Chim Acta. 2021. https://doi.org/10.1016/j.cca.2021.10.013.
34. Shan Y, Zhou P, Zhou Q, Yang L. Extracellular vesicles in the progression and therapeutic resistance of nasopharyngeal carcinoma. Cancers. 2022. https://doi.org/10.3390/cancers14092289.
35. Wu L-Z, Zou Y, Wang B-R, Ni H-F, Kong Y-G, Hua Q-Q, et al. Enhancing nasopharyngeal carcinoma cell radiosensitivity by suppressing AKT/mTOR via CENP-N knockdown. J Transl Med. 2023. https://doi.org/10.1186/s12967-023-04654-x.
36. Ieranò C, Righelli D, D'Alterio C, Napolitano M, Portella L, Rea G, et al. In PD-1+ human colon cancer cells NIVOLUMAB promotes survival and could protect tumor cells from conventional therapies. J Immunother Cancer. 2022. https://doi.org/10.1136/jitc-2021-004032.
37. You B, Cao X, Shao X, Ni H, Shi S, Shan Y, et al. Clinical and biological significance of HAX-1 overexpression in nasopharyngeal carcinoma. Oncotarget Impact J. 2016. https://doi.org/10.18632/oncotarget.7274.
38. Yan J, Wang M, Lv S, Chen D, Wu Z, Zhou D, et al. SiATG5-loaded cancer cell membrane-fused liposomes induced increased uptake of albumin-bound chemotherapeutics by pancreatic cancer cells. J Control Release. 2024. https://doi.org/10.1016/j.jconrel.2024.01.055.
39. Wu Z, Wu Y, Wang M, Chen D, Lv J, Yan J, et al. FAP-activated liposomes achieved specific macropinocytosis uptake by pancreatic stellate cells for efficient desmoplasia reversal. Chem Eng J. 2024. https://doi.org/10.1016/j.cej.2024.153369.
40. Yang X, Ren H, Li Z, Peng X, Fu J. Combinations of radiotherapy with immunotherapy in nasopharyngeal carcinoma. Int Immunopharmacol. 2023. https://doi.org/10.1016/j.intimp.2023.111094.
41. Yeo ELL, Li YQ, Soo K-C, Wee JTS, Chua MLK. Combinatorial strategies of radiotherapy and immunotherapy in nasopharyngeal carcinoma. Chin Clin Oncol. 2018. https://doi.org/10.21037/cco.2018.04.05.
42. Wang X, Huang J, Chen W, Li G, Li Z, Lei J. The updated role of exosomal proteins in the diagnosis, prognosis, and treatment of cancer. Exp Mol Med. 2022. https://doi.org/10.1038/s12276-022-00855-4.
43. Liu K, Kong L, Cui H, Zhang L, Xin Q, Zhuang Y, et al. Thymosin α1 reverses oncolytic adenovirus-induced M2 polarization of macrophages to improve antitumor immunity and therapeutic efficacy. Cell Rep Med. 2024. https://doi.org/10.1016/j.xcrm.2024.101751.
44. Cheng H, Bai J, Zhou X, Chen N, Jiang Q, Ren Z, et al. Electrical stimulation with polypyrrole-coated polycaprolactone/silk fibroin scaffold promotes sacral nerve regeneration by modulating macrophage polarisation. Biomater Transl. 2024. https://doi.org/10.12336/biomatertransl.2024.02.006.
45. Zhang B, Miao T, Shen X, Bao L, Zhang C, Yan C, et al. EB virus-induced ATR activation accelerates nasopharyngeal carcinoma growth via M2-type macrophages polarization. Cell Death Dis. 2020. https://doi.org/10.1038/s41419-020-02925-9.
46. Chen R-H, Xiao Z-W, Yan X-Q, Han P, Liang F-Y, Wang J-Y, et al. Tumor cell-secreted ISG15 promotes tumor cell migration and immune suppression by inducing the macrophage M2-like phenotype. Front Immunol. 2020. https://doi.org/10.3389/fimmu.2020.594775.
47. Ren W, Hou J, Yang C, Wang H, Wu S, Wu Y, et al. Extracellular vesicles secreted by hypoxia pre-challenged mesenchymal stem cells promote non-small cell lung cancer cell growth and mobility as well as macrophage M2 polarization via miR-21-5p delivery. J Exp Clin Cancer Res. 2019. https://doi.org/10.1186/s13046-019-1027-0.
48. Lin Y-X, Wang Y, Ding J, Jiang A, Wang J, Yu M, et al. Reactivation of the tumor suppressor PTEN by mRNA nanoparticles enhances antitumor immunity in preclinical models. Sci Transl Med. 2021. https://doi.org/10.1126/scitranslmed.aba9772.
49. Chang ET, Ye W, Zeng Y-X, Adami H-O. The evolving epidemiology of nasopharyngeal carcinoma. Cancer Epidemiol Biomarkers Prev. 2021. https://doi.org/10.1158/1055-9965.epi-20-1702.
50. Sun G, Liu F, Lesany M, Nemati S. Comprehensive analysis of recently discovered lncRNA-associated competing endogenous RNA network in nasopharyngeal carcinoma. Pathol Res Pract. 2024. https://doi.org/10.1016/j.prp.2024.155314.
51. Cai C, Lv W, Chi F, Zhang B, Zhu L, Yang G, et al. Prognostic generalization of multi-level CT-dose fusion dosiomics from primary tumor and lymph node in nasopharyngeal carcinoma. Med Phys. 2022. https://doi.org/10.1002/mp.16044.
52. Hao R, Yu Z, Du J, Hu S, Yuan C, Guo H, et al. A high-throughput nanofluidic device for exosome nanoporation to develop cargo delivery vehicles. Small. 2021. https://doi.org/10.1002/smll.202102150.
53. Akilu S, Sharma KV, Baheta AT, Kanti PK, Paramasivam P. Machine learning analysis of thermophysical and thermohydraulic properties in ethylene glycol- and glycerol-based SiO2 nanofluids. Sci Rep. 2024. https://doi.org/10.1038/s41598-024-65411-8.
54. Jakeer S, Basha HT, Reddy SRR, Abbas M, Alqahtani MS, Loganathan K, et al. Entropy analysis on EMHD 3D micropolar tri-hybrid nanofluid flow of solar radiative slendering sheet by a machine learning algorithm. Sci Rep. 2023. https://doi.org/10.1038/s41598-023-45469-6.
55. Xie Q-H, Zheng J-Q, Ding J-Y, Wu Y-F, Liu L, Yu Z-L, et al. Exosome-mediated immunosuppression in tumor microenvironments. Cells. 2022. https://doi.org/10.3390/cells11121946.
56. Zhang F, Jiang J, Qian H, Yan Y, Xu W. Exosomal circRNA: emerging insights into cancer progression and clinical application potential. J Hematol Oncol. 2023. https://doi.org/10.1186/s13045-023-01452-2.
57. Li B, Cao Y, Sun M, Feng H. Expression, regulation, and function of exosome-derived miRNAs in cancer progression and therapy. FASEB J. 2021. https://doi.org/10.1096/fj.202100294rr.
58. Paskeh MDA, Entezari M, Mirzaei S, Zabolian A, Saleki H, Naghdi MJ, et al. Emerging role of exosomes in cancer progression and tumor microenvironment remodeling. J Hematol Oncol. 2022. https://doi.org/10.1186/s13045-022-01305-4.
59. Fan L, Liu C, Chen X, Zheng L, Zou Y, Wen H, et al. Exosomes-loaded electroconductive hydrogel synergistically promotes tissue repair after spinal cord injury via immunoregulation and enhancement of myelinated axon growth. Adv Sci. 2022. https://doi.org/10.1002/advs.202105586.

60. Holas P, Kamińska J. Mindfulness meditation and psychedelics: potential synergies and commonalities. Pharmacol Rep. 2023. https://doi.org/10.1007/s43440-023-00551-8.
61. Jing Z, Liu N, Zhang Z, Hou X. Research progress on plant responses to stress combinations in the context of climate change. Plants. 2024. https://doi.org/10.3390/plants13040469.
62. Cao W, Li J, Yang K, Cao D. An overview of autophagy: mechanism, regulation and research progress. Bull Cancer. 2021. https://doi.org/10.1016/j.bulcan.2020.11.004.
63. Bergholz JS, Wang Q, Wang Q, Ramseier M, Prakadan S, Wang W, et al. PI3Kβ controls immune evasion in PTEN-deficient breast tumours. Nature. 2023. https://doi.org/10.1038/s41586-023-05940-w.
64. Dariya B, Aliya S, Merchant N, Alam A, Nagaraju GP. Colorectal cancer biology, diagnosis, and therapeutic approaches. Crit Rev Oncog. 2020. https://doi.org/10.1615/critrevoncog.2020035067.

Publisher’s Note